

# A Scaling Law for Synthetic-to-Real Transfer: A Measure of Pre-Training

**Hiroaki Mikami\***

Preferred Networks, Inc.  
mhiroaki@preferred.jp

**Kenji Fukumizu\***

Institute of Statistical Mathematics  
/Preferred Networks, Inc.  
fukumizu@ism.ac.jp

**Shogo Murai**

Preferred Networks, Inc.  
murai@preferred.jp

**Shuji Suzuki**

Preferred Networks, Inc.  
ssuzuki@preferred.jp

**Yuta Kikuchi**

Preferred Networks, Inc.  
kikuchi@preferred.jp

**Taiji Suzuki**

The University of Tokyo/AIP-RIKEN  
taiji@mist.i.u-tokyo.ac.jp

**Shin-ichi Maeda**

Preferred Networks, Inc.  
ichi@preferred.jp

**Kohei Hayashi\*<sup>†</sup>**

Preferred Networks, Inc.  
hayasick@preferred.jp

## Abstract

Synthetic-to-real transfer learning is a framework in which we pre-train models with synthetically generated images and ground-truth annotations for real tasks. Although synthetic images overcome the data scarcity issue, it remains unclear how the fine-tune performance scales with pre-trained models, especially in terms of pre-training data size. In this study, we collect a number of empirical observations and uncover the secret. Through experiments, we observe a simple and general scaling law that consistently describes learning curves in various tasks, models, and complexities of synthesized pre-training data. Further, we develop a theory of transfer learning for a simplified scenario and confirm that the derived generalization bound is consistent with our empirical findings.

## 1 Introduction

The success of deep learning in computer vision relies on the availability of large data sets. If the target task provides limited data, the framework of transfer learning is preferably employed. A typical scenario of transfer learning is to pre-train a model for a similar or even different task (e.g., ImageNet [49]) and fine-tune the model for the target task with smaller data. The data scalability, however, is again a bottleneck of supervised pre-training. While computational power and model size have grown exponentially, the standard data size for pre-training remains the same [52], mainly because of the cost to collect images and annotations.

*Synthetic-to-real transfer learning* — pre-training with synthetic images for real tasks — is a promising approach for data scalability [51, 40, 18, 56, 25, 8, 11]. By combining various conditions, such as 3D models, textures, light conditions, and camera poses, we can conceptually generate an infinite number of images with ground-truth annotations. Despite the empirical success, however, the systematic understanding of how synthetic-to-real transfer learning works has been critically lacking. For example, in a standard learning setting, a “power law”-like relationship called *scaling law* often

\*Equal contribution

<sup>†</sup>Corresponding author

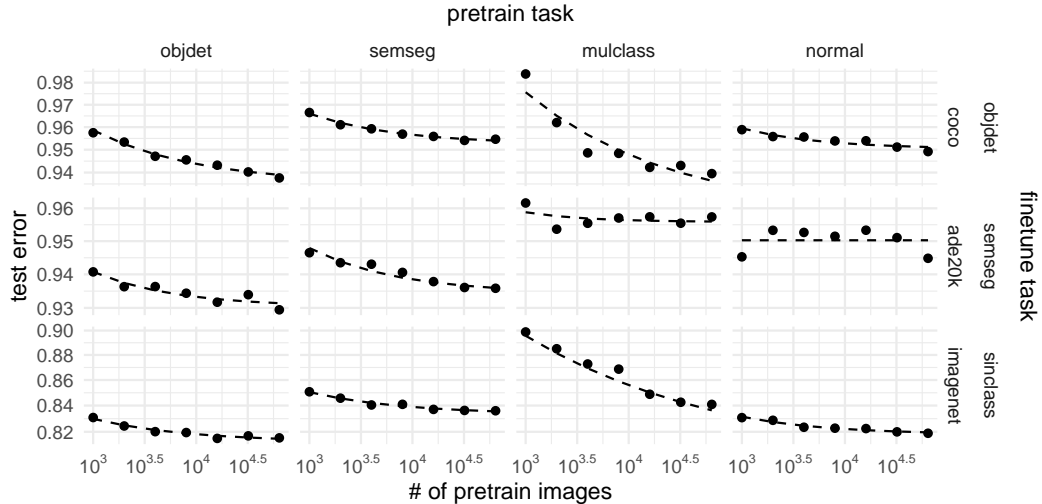


Figure 1: Empirical results of syn-to-real transfer learning for different tasks. We conducted four pre-training tasks: object detection (objdet), semantic segmentation (semseg), multi-label classification (mulclass), surface normal estimation (normal), and three fine-tuning tasks for benchmark data sets: object detection for MS-COCO, semantic segmentation for ADE20K, and single-label classification (sinclass) for ImageNet. The y-axis indicates the test error for each fine-tuning task. Dots indicate empirical results and dashed lines indicate fitted curves (1). For more details, see Section 4.1.

holds between data size and generalization errors [48, 31]. Questions then arise: For pre-training with synthetic images, does a similar law hold? How does the pre-training data complexity affect? What is the model size effect?

To answer these questions, we propose an equation that describes the generalization error in terms of the pre-training and fine-tuning data size. Our main finding is that, when the fine-tuning data size is fixed and pre-training data size  $n$  is not too small (say,  $n > 1000$ ), the generalization error of the fine-tuning task is well explained by

$$\text{test error} \simeq Dn^{-\alpha} + C, \quad (1)$$

where coefficient  $D > 0$  and *pre-training rate*  $\alpha > 0$  describe the convergence speed of pre-training, and *transfer gap*  $C \geq 0$  determines the lower limit of the error. We can predict how large the pre-training data should be to achieve the desired accuracy by estimating the parameters  $\alpha, C$  from the empirical results. Additionally, we analyze transfer learning theoretically using the recent advance based on the neural tangent kernel [45] and confirm that the above law agrees with the generalization analysis.

Our contributions are summarized as follows.

- From motivated empirical results and theoretical hints, we elicit the law of generalization scale in terms of pre-training and fine-tuning data sizes.
- We confirm the derived law explains the empirical results for a variety of different settings in terms of pre-training/fine-tuning tasks, model size, and data complexity (e.g., Figure 1). Furthermore, we demonstrate that the law enables us to assess how pre-training is effective via the estimated parameters.
- We theoretically derive a generalization bound for a general transfer learning setting and confirm its agreement with our empirical findings.

## 2 Related Work

**Supervised pre-training for visual tasks** Many empirical studies have been conducted where the fine-tuning task performance scales with pre-training data (and model) size. For example, Huh et al. [28] studied the scaling behavior on ImageNet pre-trained models. Beyond ImageNet, Sun et al. [52]

studied the effect of pre-training with pseudo-labeled large-scale data and observed a logarithmic scaling behavior. Similar results were observed by Kolesnikov et al. [32].

Adaptivity to different domains or tasks is an essential topic. Kornblith et al. [33] showed that the accuracy on ImageNet is positively correlated with the accuracy on different classification data sets using ImageNet pre-trained models. Zamir et al. [59] intensively investigated what pre-training task is helpful to what fine-tuning task using an indoor-scene data set. Mensink et al. [37] conducted similar experiments but they performed validations using multiple data sets including synthetic images for pre-training/fine-tuning. Our experimental setting is located in the middle of these; we used a single data set for pre-training but multiple for fine-tuning.

Several recent studies have reported the limitations of supervised pre-training. Most notably, the gain from pre-training can easily vanish [20, 41] or a target task accuracy even degrade [62] if we have large enough data for fine-tuning. However, there are cases such as few-shot learning [54] where fine-tuning data are extremely limited, and thus supervised pre-training is necessary for practice.

**Theory of transfer learning** Although analysis of transfer learning using learning theory was attempted decades ago (e.g., [6]), the effect of pre-training data size has not been considered until recently. Du et al. [15] and Tripuraneni et al. [57] derived the error bound of a fine-tuning task in an additive form as  $O(An^{-1/2} + Bs^{-1/2})$  with pre-training data size  $n$  and fine-tuning data size  $s$  with coefficients  $A, B$  based on complexity analysis.

We emphasize that the additive bound is not directly applicable to our case, mainly because the protocol of transfer learning is different. During fine-tuning, they optimize a head network while a backbone network is frozen. Thus, the additive bound is legitimate because the pre-training effect should remain even if the model is fine-tuned with large data. However, we optimize both head and backbone during fine-tuning. In that case, the effect of pre-training is converted into initial values. To analyze the effect of initial values, we have to take into account the learning dynamics of a neural network. Our analysis actually captures this aspect and we derive a bound in a *multiplicative* form; see Sections 3.1 and 5 for more details.

**Neural scaling laws** There are a lot of prior studies that investigate the scaling behavior of generalization error (e.g., [2]). For modern neural networks, Hestness et al. [24] observed the power-law behavior of generalization for different application domains (language, image, and speech) with respect to the training size. Rosenfeld et al. [48] constructed a predictive form for the power-law behavior with data and model scaling. Kaplan et al. [31] pushed forward this direction in the language domain, describing that the generalization of transformers obeys the power law in terms of a compute budget in addition to data and model sizes. Since then, similar scaling laws have been discovered in other data domains [21]. Theoretical analysis was also attempted [29, 4].

This study is inspired by Hernandez et al. [23], who studied the scaling phenomena for transfer learning. One key difference is that Hernandez et al. focused on fine-tuning data size as a scaling factor, while we focus on pre-training data size. Further, Hernandez et al. found scaling laws of the transferred effective data, which is converted data amount necessary to achieve the same performance gain by pre-training. In contrast, Eq. (1) directly explains an absolute error at a fine-tuning task. Other differences include task domains (language vs. vision) and architectures (transformer vs. CNN).

**Synthetic-to-real generalization** The utility of synthetic images as supervised data for computer vision tasks has been continuously studied by many researchers [51, 40, 18, 56, 25, 8, 11, 41, 13, 39, 26]. These studies found positive evidence that synthetic images are helpful. In addition, they demonstrated how data complexity, induced by e.g., light randomization, affects the final performance. For example, Newell and Deng [41] investigated how the recent self-supervised methods perform well as a pre-training task to improve the performance of downstream tasks. They utilized synthetic images with several randomizations to generate large and controlled data sets for a comprehensive comparison. In this paper, we reconfirm the same tendency and describe the degree of the effect under the lens of the scaling law (1).

### 3 Methods

In this study, we employ the following protocol for transfer learning. First, we pre-train a model that consists of backbone and head networks until convergence, and we select the best model in terms of the validation error of the pre-training task. Then, we extract the backbone and add a new head to fine-tune all model parameters.

For notations, let  $L(n, s) \geq 0$  be the test error of a fine-tuning task with pre-training data size  $n$  and fine-tuning data size  $s$ . The task names of object detection, semantic segmentation, multi-label classification, single-label classification, and surface normal estimation are abbreviated as `objdet`, `semseg`, `mulclass`, `sinclass`, and `normal`, respectively. The settings for transfer learning are denoted by arrows. For example, `objdet`→`semseg` indicates that a pre-training task is object detection, and a fine-tuning task is semantic segmentation.

#### 3.1 Deduction of scaling law

We make the following four requirements to formalize the scaling law.

**Requirement 1.** *The fine-tuning error is decomposed as  $L(n, s) = \mathcal{R}(n, s) + \mathcal{E}$ , ( $\mathcal{E} \geq 0$ ).*

**Requirement 2.**  *$\mathcal{R}(n, s)$  can be written as  $\mathcal{R}(n, s) = f(n^{-\alpha}, s^{-\beta}) \geq 0$  with a simple function  $f$ .*

**Requirement 3.**  $\lim_{s \rightarrow \infty} \mathcal{R}(n, s) = 0$ .

**Requirement 4.**  $\lim_{n \rightarrow \infty} \mathcal{R}(n, s) = \text{const.}$

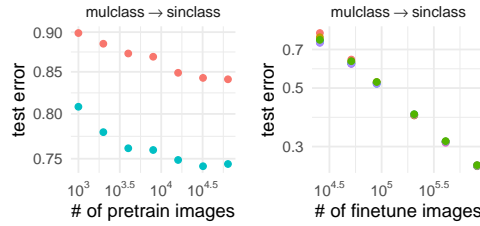


Figure 2: Asymmetric scaling.

Requirements 1 and 2 follow the standard form of generalization given by the learning theory (e.g., PAC learning [38]). Namely, the error is decomposed into reducible part  $\mathcal{R}$  and irreducible parts  $\mathcal{E}$  as  $L(n, s) = \mathcal{R} + \mathcal{E}$ , where  $\mathcal{R}$  depends on the polynomial decay with respect to the fine-tuning data size  $s$ . Further, we hypothesize that the effect of pre-training data size  $n$  is embedded in the reducible part as a polynomial decay form, as pre-training helps reduce the fine-tuning error faster.

Requirements 3 and 4 constrain how pre-training effect  $n^{-\alpha}$  and fine-tuning effect  $s^{-\beta}$  interact with each other. When we fix the pre-training data size  $n$  and increase the fine-tuning data size  $s$ , this is the case the standard scaling law [31] holds (pre-training only modifies initial weights). Hence the reducible error  $\mathcal{R}$  should go to zero (Requirement 3). In contrast, when  $s$  is fixed,  $\mathcal{R}$  is not necessarily going to zero, especially when a pre-training task is largely irrelevant (Requirement 4). Empirical results also support the asymmetry of the pre-training and fine-tuning effects. Figure 2 (replicated from Figure 4) presents the log-log plot of scaling curves in the case of `mulclass`→`sinclass` with respect to pre-training/fine-tuning data size, where each color indicates a different fine-tuning/pre-training data size. The left panel shows the pre-training effect diminishes for large  $n$ , while the right panel shows the fine-tuning effect follows a power law.

To satisfy Requirement 3, it is reasonable to formulate the law in a multiplicative form  $\mathcal{R}(n, s) = g(n^{-\alpha})h(s^{-\beta})$  rather than the additive form  $g(n^{-\alpha}) + h(s^{-\beta})$ . In addition, a simple choice for Requirement 4 is to introduce an irreducible term as  $g(n^{-\alpha}) \propto n^{-\alpha} + \gamma$  such that the effect of  $n$  cannot be lower than  $\gamma$ . By combining these, we obtain

$$L(n, s) = \delta(n^{-\alpha} + \gamma)s^{-\beta} + \mathcal{E}, \quad (2)$$

where  $\alpha, \beta > 0$  are decay rates for pre-training and fine-tuning, respectively,  $\gamma \geq 0$  is a constant,  $\delta > 0$  is a coefficient, and  $\mathcal{E} \geq 0$  is an optimal error that is irreducible owing to the noise. If we have sufficient observations, we can estimate these parameters by using the nonlinear least squares method.

**Simplification for empirical estimation** When the number of observed points are limited in experimental studies, further simplification is necessary for numerical stability of empirical estimation. In particular, when  $s$  is small (a standard setting of few-shot learning), it is not realistic to conduct experiments for many different  $s$ , and estimating all parameters in (2) could be ill-conditioned. In this case, a practical solution is to simplify (2) by eliminating  $s$ -dependent terms by setting  $D = \delta s^{-\beta}$



and  $C = \delta\gamma s^{-\beta} + \mathcal{E}$ , which gives (1). Then, we can estimate  $D$  and  $C$  as they are independent parameters (rather than depending on  $s$ ). We hereafter refer to (2) as the full scaling law to distinguish from (1).

### 3.2 Experimental settings

The experiments were conducted on an in-house cluster containing NVIDIA V100 GPUs. The total amount of computation was approximately 1700 GPU days (200 for image rendering, 1300 for pre-training, and 200 for fine-tuning). Code and pre-trained models are available at <https://github.com/pfnnet-research/cg-transfer>.

**Pre-training data:** We generated synthetic image data sets by BlenderProc [12], an image renderer that can handle several domain randomization methods. For rendering, we used the setting of the BOP challenge 2020 [27] as our default setting. We used 172 3D models, where ten objects appeared on average for each image. We applied texture randomization for walls and a floor, randomization for area and point lights, and randomization for the camera. Teacher signals (e.g., class labels for a classification task) were generated along with the images. We prepared two data sets of different sizes: 64 thousand and 1.28 million images. Because the learning curves of both data sets were similar, we showed the results of 64 thousand in the main paper and deferred the latter results in Appendix C.2.

**Pre-training:** We prepared four tasks: multi-label classification, object detection, semantic segmentation, and surface normal estimation. We used ResNet-based models, where backbones were ResNet-50, unless otherwise specified, and the head networks were customized for each task. We trained all models for the same fixed number of iterations depending on pre-training tasks and selected the best models as pre-trained models, which were validated by another 1000 synthetic images generated in the same way.

**Fine-tuning:** We employed three data sets: ImageNet (ILSVRC 2012) [49] for single-label classification, MS-COCO [34] for object detection, and ADE20K [60] for semantic segmentation. The number of images used was 1% of each data set (roughly, 12 thousand for ImageNet, a thousand for COCO, and 2 hundred for ADE20K). We fine-tuned the pre-trained models with these subsets of data for a fixed number of iterations and reported the error metrics for validation sets at the last iteration. The metrics were top-1 accuracy for classification, mean mAP for MS-COCO, and mean IoU for ADE20K. These metrics take their values from 0 to 1, and we converted them into errors such as 1 - accuracy.

**Curve fitting:** After obtaining the empirical errors, we estimated the parameters of (1) by nonlinear least squares in the log-log space, i.e., we solved the minimization problem  $\min_{\alpha, C, D} \sum_i |\log \hat{L}(n_i, s) - \log(Dn_i^{-\alpha} + C)|^2$  with a fixed fine-tuning data size  $s$  and pre-training data sizes  $n_i = 2^i \times 1000$  for data point index  $i = 0, \dots, 6$  where  $\hat{L}$  denotes an observed error. Note that, except for the setting in Section 4.3, we fitted the curves independently for every different data sets, tasks, and  $s$ . All the results including Figure 1 were shown as log-log plots.

In the experiments, we empirically encountered some instability between  $D$  and  $\alpha$ . We fixed  $D = 0.48$  by the median values of  $D$ 's for all the settings and estimated  $\alpha$  and  $C$  independently for each case. We explain this procedure with more details in Appendix D.

## 4 Experimental Results and Scaling Laws

### 4.1 Scaling law universally describes across different pre-training/fine-tuning tasks

Figure 1 shows the test errors of each fine-tuning task and fitted learning curves with Eq. (1), which describes the effect of pre-training data size  $n$  for all combinations of pre-training and fine-tuning tasks. In most cases, the scaling law fits with the empirical fine-tuning test errors with high accuracy. The fittings of `mulclass`→`semseg` and `normal`→`semseg` are less accurate than the others. We empirically observed that the score of semantic segmentation at fine-tuning had much higher variance than other fine-tuning tasks, and this may cause under-fittings because of the instability.

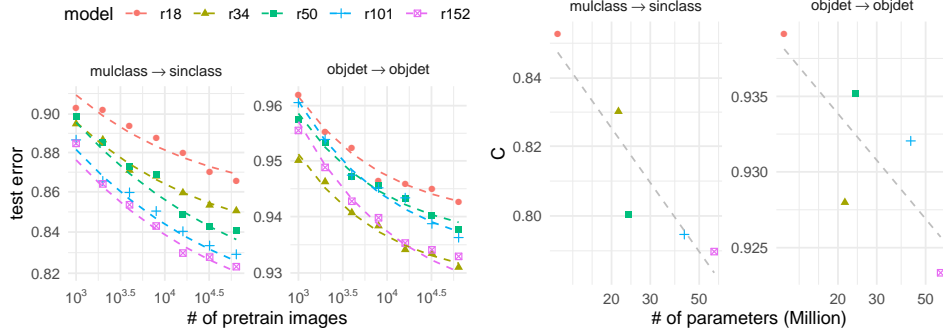


Figure 3: Effect of model size. Best viewed in color. **Left:** The scaling curves for mulclass→sinclass and objdet→objdet cases. The meanings of dots and lines are the same as those in Figure 1. **Right:** The estimated  $C$  (y-axis) versus the model size (x-axis). the dots are estimated values, and the lines are linear fittings of them.

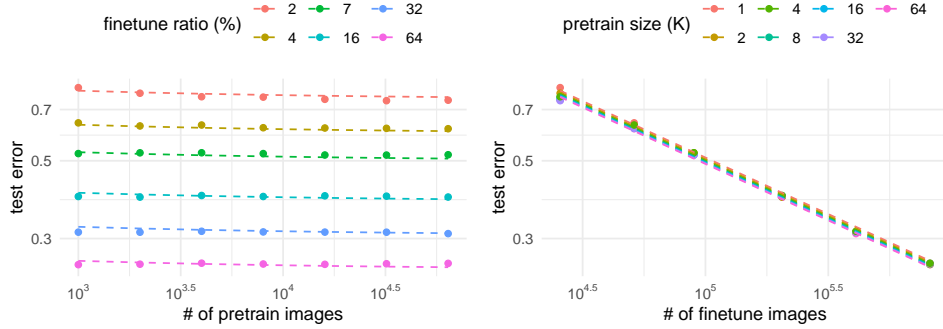


Figure 4: Empirical and fitting results for various pre-train and fine-tune data sizes in mulclass→sinclass. All curves are fitted using the full law (2). Best viewed in color. **Left:** Effect of pre-training data size (x-axis) for fixed fine-tuning data sizes. **Right:** Effect of fine-tuning data size (x-axis) for fixed pre-training data sizes.

#### 4.2 Bigger models reduce the transfer gap

We compared various ResNet models as backbones in mulclass→sinclass and objdet→objdet to observe the effects of model size. Figure 3 (left) shows the curves of scaling laws for the pre-training data size  $n$  for different sizes of backbone ResNet- $x$ , where  $x \in \{18, 34, 50, 101, 152\}$ . The bigger models attain smaller test errors. Figure 3 (right) shows the values of the estimated transfer gap  $C$ . The results suggest that there is a roughly power-law relationship between the transfer gap and model size. This agrees with the scaling law with respect to the model size shown by Hernandez et al. [23].

#### 4.3 Full scaling law collectively relates pre-training and fine-tuning data size

Next, we verify the validity of the full scaling law (2). In the mulclass→sinclass setting with ResNet-50, we changed the fine-tuning data size from 2% to 64% of the ImageNet.<sup>3</sup> We then fitted all results by a single equation (2) to estimate the parameters except the irreducible loss  $\mathcal{E}$  (we assumed  $\mathcal{E} = 0$  from the preliminary results in Figure 2). The results in Figure 4 show that all empirical test errors are explained remarkably well by Eq. (2), which has only four parameters to fit in this case. The estimated parameters are  $\alpha = 0.544$ ,  $\beta = 0.322$ ,  $\gamma = 0.478$ , and  $\delta = 41.8$ .

<sup>3</sup>ImageNet contains a class imbalance problem. If we use 100% of the ImageNet, we cannot provide the same sample size per class. To eliminate the effect of class imbalance, we made the sampling ratio to keep the balance up to 64% and excluded the case of 100%.

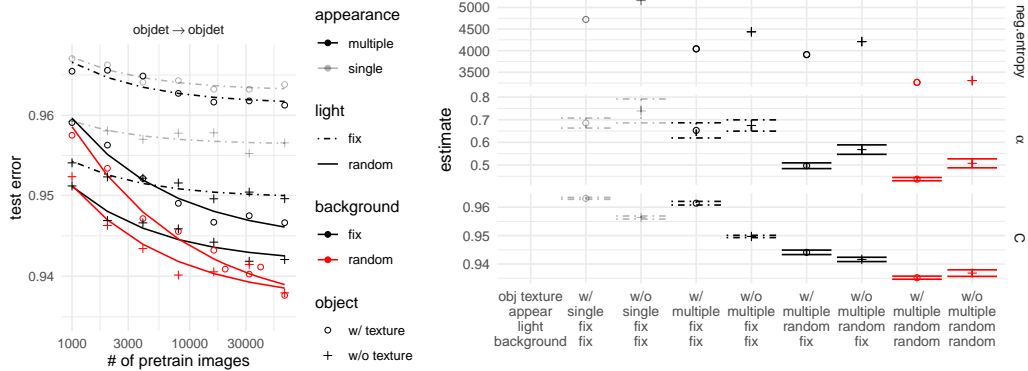


Figure 5: Effect of synthetic image complexity. Best viewed in color. **Left:** Scaling curves of different data complexities. **Right:** Estimated parameters. The error bars represent the standard error of the estimate in least squares.

#### 4.4 Data complexity affects both pre-training rate and transfer gap

We examined how the complexity of synthetic images affects fine-tuning performance. We controlled the following four rendering parameters: *Appearance*: Number of objects in each image; *single* or *multiple* (max 10 objects). *Light*: Either an area and point light is randomized or fixed in terms of height, color, and intensity. *Background*: Either the textures of floor/wall are randomized or fixed. *Object texture*: Either the 3D objects used for rendering contain texture (w/) or not (w/o). Indeed, the data complexity satisfies the following ordered relationships: *single* < *multiple* in *appearance*, *fix* < *random* in *light* and *background*, and *w/o* < *w/* in *object texture*<sup>4</sup>. To quantify the complexity, we computed the negative entropy of the Gaussian distribution fitted to the last activation values of the backbone network. For this purpose, we pre-trained ResNet-50 as a backbone with MS-COCO for 48 epochs and computed the empirical covariance of the last activations for all the synthetic data sets.

The estimated parameters are shown in Figure 5, which indicates the following (we discuss the implications of these results further in Section 6.1).

- Data complexity controlled by the rendering settings correlates with the negative entropy, implying the negative entropy expresses the actual complexity of pre-training data.
- Pre-training rate  $\alpha$  correlates with data complexity. The larger complexity causes slower rates of convergence with respect to the pre-training data size.
- Transfer gap  $C$  mostly correlates negatively with data complexity, but not for *object texture*.

As discussed in Section 3.2, we have fixed the value of  $D$  to avoid numerical instability, which might cause some bias to the estimates of  $\alpha$ . We postulate, however, the value of  $D$  depends mainly on the fine-tuning task and thus has a fixed value for different pre-training data complexities. This can be inferred from the theoretical analysis in Appendix E.5: the exponent  $\beta$  in the main factor  $s^{-\beta}$  of  $D$  does not depend on the pre-training data distribution but only on the fine-tuning task or the pre-training true mapping. Thus, the values of  $D$  should be similar over the different complexities, and the correlation of  $\alpha$  preserves.

## 5 Theoretical Analysis

This section provides a theoretical analysis of transfer learning in a simplified setting and derives a generalization bound, which agrees well with the full scaling law (2). The analysis relies on the recent work on the convergence and generalization bounds by Nitanda and Suzuki [45], and extends it to the case of the pre-training/fine-tuning scenario. The framework in [45] is suitable for our purpose since we can consider the initialization of learning and do not need a lower bound of eigenvalue unlike [3]. All details will be presented in Appendix E.

<sup>4</sup>The object category of w/o is a subset of w/, and w/ has a strictly higher complexity than w/o.

In pre-training, the target function to learn is  $\varphi_0$  with training data  $(\tilde{x}_i, \tilde{y}_i)_{i=1}^{T_0}$ , where  $\tilde{x}_i \sim \rho_X$  is i.i.d. and  $\tilde{y}_i = \varphi_0(\tilde{x}_i)$ . In fine-tuning, the network is initialized by the parameter of the pre-training and the whole parameter is updated according to the stochastic gradient descent (SGD). The target function in the fine-tuning is given by

$$\varphi(x) = \varphi_0(x) + \varphi_1(x), \quad (3)$$

To simplify the theoretical analysis, we assume noiseless training data, that is, the training data are given by  $(x_j, y_j)_{j=1}^{T_1}$ , where  $x_i \sim \rho_X$  is i.i.d. and  $y_j = \varphi(x_j)$ . Also, we assume  $\|\tilde{x}_i\|_2 = \|x_j\|_2 = 1$ ,  $\tilde{y}_i, y_j \in [0, 1]$ , and a simple scalar-valued two-layer neural network model:

$$g_\Theta(x) = \frac{1}{\sqrt{M}} \sum_{r=1}^M a_r \sigma(b_r^T x), \quad (4)$$

where  $\Theta = (a_r, b_r)$  is the parameter and the activation  $\sigma$  is second differentiable so that  $\sigma'$  and  $\sigma''$  are bounded and  $|\sigma(u)| \leq 1 + |u|$ . We omit the bias term; however, with obvious modification, it is not difficult to include it.

Let  $(\gamma_\ell)_{\ell=1}^\infty$  ( $\gamma_1 \geq \gamma_2 \geq \dots > 0$ ) denote the eigenvalues of the covariance operator  $\Sigma_\infty := E_{X \sim \rho_X} [k_\infty(\cdot, X) \otimes k_\infty(X, \cdot)^*]$ , where  $k_\infty$  is the neural tangent kernel [30, 45]. As the typical parameters for describing generalization bounds [9], we assume (A1) there is  $\xi > 1$  such that  $\gamma_\ell \sim \ell^{-\xi}$ , and (A2) there are  $r_0, r_1 \in [1/2, 1]$  such that  $\varphi_i \in \mathcal{R}(\Sigma_\infty^{r_i})$  ( $i = 0, 1$ ), where  $\mathcal{R}$  denotes the range. The parameter  $\xi$  represents the complexity of the hypothesis class  $\mathcal{H}_\infty$ , which is the reproducing kernel Hilbert space defined by  $k_\infty$ , and  $r_i$  is the degree of smoothness of  $\varphi_i$ .

As in [45], we consider the averaged SGD (ASGD), where one training sample  $(x_t, y_t)$  is given at every time step for SGD, and the parameters  $\Theta^{(0)}, \dots, \Theta^{(T)}$  are averaged to obtain the final result  $\bar{\Theta}^{(T)} := (T+1)^{-1} \sum_{t=0}^T \Theta^{(t)}$ . For both the pre-training and fine-tuning, the objective function to minimize is the following regularized empirical risk:

$$L(\Theta) := \frac{1}{2} \sum_i (y_i - g_\Theta(x_i))^2 + \frac{\lambda}{2} \{ \|a - a^{(0)}\|_2^2 + \sum_r \|b_r - b_r^{(0)}\|_2^2 \}, \quad (5)$$

where  $\Theta^{(0)} = (a_r^{(0)}, b_r^{(0)})_{r=1}^M$  are the initial parameters for either the pre-training or fine-tuning, and  $\lambda = \lambda_0$  and  $\lambda_1$  are the regularization coefficients for pre-training and fine-tuning, respectively.

Nitanda and Suzuki [45] show that, if the regularization parameter is optimized, the ASGD for pre-training yields the generalization bound

$$\hat{R}_0 := E \|\hat{\varphi}_0 - \varphi_0\|_{L_2(\rho_X)}^2 \leq c_M + A_0 T_0^{-\frac{2r_0\xi}{2r_0\xi+1}} \quad (T_0 \rightarrow \infty), \quad (6)$$

where  $\hat{\varphi}_0$  is the final network after  $T_0$  data. The constant  $c_M$  is arbitrarily small if  $M \rightarrow \infty$ , and  $A_0$  is a constant factor that depends on  $\varphi_0$ . This bound is known to be of optimal rate in terms of  $T_0$ .

Extending [45], we obtain the bound of the generalization error for transfer learning:

**Theorem 1 (Informal).** *Suppose Assumptions (A1) and (A2) hold. Fine-tune the network after pre-training that satisfies Eq. (6). Then, for any  $\varepsilon > 0$ , there exists  $M_0 \in \mathbb{N}$  such that for any  $M \geq M_0$ , the following holds with high probability:*

$$\begin{aligned} E \|g_{\bar{\Theta}^{(T_1)}} - \varphi\|_{L_2(\rho_X)}^2 &\leq \varepsilon + c_0 \lambda_1^{2r_0} + c_1 \lambda_1^{2r_1} + \frac{c_2}{T_1 + 1} \{ \lambda_1^{-1} \hat{R}_0 + a_{1,1} \lambda_1^{2r_1-1} + a_{1,2} \} \\ &\quad + \frac{c_3}{(T_1 + 1)^2 \eta_1^2} \{ \lambda_1^{-2} \hat{R}_0 + a_{2,1} \lambda_1^{2r_1-2} + a_{2,2} \lambda_1^{-1} \} + \frac{c_4}{T_1 + 1} \lambda_1^{-1/\xi}, \end{aligned} \quad (7)$$

where  $\eta_1$  is a learning rate of ASGD, and constants  $c_i, a_{i,k}$  depend on the function norms of  $\varphi_0, \varphi_1$ .

We consider the convergence rate for  $T_1 \rightarrow \infty$  with  $\lambda_1$  and  $\eta_1$  depending on  $T_1$ . We focus on the situation where the regularization  $\lambda_1$  is larger than usual learning, reflecting the transfer learning setting, where the information of pre-training should be preserved. Specifically, we assume  $\lambda_1 = \Omega(T_1^{-\frac{2r_1\xi}{2r_1\xi+1}})$ . In this case, the terms of rates  $\lambda_1^{2r_0}$ ,  $\lambda_1^{2r_1}$ ,  $T_1^{-1} \lambda_1^{-1}$ , and  $T_1^{-2} \eta_1^{-2} \lambda_1^{-2}$  can be dominant.

Among the possible cases discussed in Section E.5, we here show the convergence rate only for  $r_0 \geq r_1$  and  $\eta = T_1^{-\zeta}$  with  $\zeta \in [\max\{r_1/(2r_1+1), (r_1\xi+1-\xi)/(2r_1\xi+1)\}, 1]$ . Details and

the other cases are shown in Appendix E. By equating two dominant terms  $\lambda_1^{2r_1}$  and  $T_1^{-2}\eta_1^{-2}\lambda_1^{-2}$ ,  $\lambda_1 = T_1^{-(1-\zeta)/(r_1+1)}\hat{R}_0^{1/(2r_1+2)}$  is optimal and

$$E\|g_{\Theta^{(T_1)}} - \varphi\|_{L^2(\rho_X)}^2 \leq \varepsilon + CT_1^{-\frac{2r_1(1-\zeta)}{r_1+1}}\hat{R}_0^{\frac{2r_1}{2r_1+2}}. \quad (8)$$

Although the current learning method is online-type, different from the one used in the previous sections, based on the fact that the ASGD achieves the optimal learning rate, we match the data size as  $T_0 = n$  and  $T_1 = s$ . Plugging Eq. (6) into Eq. (8), we obtain

$$E\|g_{\Theta^{(T_1)}} - \varphi\|_{L^2(\rho_X)}^2 \leq \varepsilon + C(c'_M + A'_0 n^{-\frac{2r_0\xi}{2r_0\xi+1} \cdot \frac{r_1}{r_1+1}})s^{-\frac{2r_1(1-\zeta)}{r_1+1}}. \quad (9)$$

It is notable that Eq. (9) has the same form as the proposed scaling law (2). This provides theoretical support to the law, while the problem settings are not exactly the same. Since  $r_1 \in [1/2, 1]$ , with a large value of  $r_0\xi$ , the exponent of  $T_0$  ranges roughly in  $[-1/2, -1/3]$ .

## 6 Conclusion and Discussion

In this paper, we studied the performance of synthetic-to-real transfer learning scales with pre-training and fine-tuning data size. Based on the experimental results, we found a scaling law (1) and its generalization (2) that explain the scaling behavior in a variety of settings in terms of pre-training/fine-tuning tasks, model sizes, and data complexities. Further, we present the theoretical error bound for transfer learning and found our theoretical bound has a good agreement with the scaling law.

### 6.1 Implication of complexity results in Section 4.4

The results of Section 4.4 suggest two things. First, data complexity (i.e., the diversity of images) largely affects the pre-training rate  $\alpha$ . This is reasonable because if we want a network to recognize more diverse images, we need to train it with more examples. Indeed, prior studies [50, 4] observed that  $\alpha$  is inversely proportional to the intrinsic dimension of the data (e.g., dimension of the data manifold), which is an equivalent concept of data complexity.

Second, the estimated values of the transfer gap  $C$  suggest that adding complexity to data is usually beneficial to decrease  $C$ , but not always. Figure 5 (right) shows that increasing complexities in terms of *appearance*, *light*, and *background* reduces the transfer gap, which implies that these rendering operations are most effective to cover the fine-tuning task that uses real images. However, the additional complexity in *object texture* works negatively. We suspect that this occurred because of *shortcut learning* [17]. Namely, adding textures to objects makes the recognition problem falsely easier because we can identify objects by textures rather than shapes. Because CNNs prefer to recognize objects by textures [16, 22], the pre-trained models may overfit to learn the texture features. Without object textures, pre-trained models have to learn the shape features because there is no other clue to distinguish the objects, and the learned features will be useful for real tasks.

Based on the above observations, we hypothesize the following relationship: Let  $x$  be an image and  $y$  be its annotation. The pre-training rate  $\alpha$  and the transfer gap  $C$  correlate with the complexity of  $p_{\text{pretrain}}(x)$ , which is the image distribution in the pre-training task; as  $p_{\text{pretrain}}(x)$  covers larger areas, the pre-training rate  $\alpha$  and the transfer gap  $C$  decrease monotonically. The difference of the decision rules in pre-training and fine-tuning tasks (i.e.,  $p_{\text{pretrain}}(y | x)$  and  $p_{\text{finetune}}(y | x)$ ) also affects the transfer gap  $C$ . Nguyen et al. [44] discussed a similar concept. Making more rigorous analysis on this will be among future works.

### 6.2 Lessons to transfer learning and synthetic-to-real generalization

Our results suggest the transfer gap  $C$  is the most crucial factor for successful transfer learning because  $C$  determines the maximum utility of pre-training. Large-scale pre-training data can be useless when  $C$  is large. In contrast, if  $C$  is negligibly small, the law becomes  $n^{-\alpha}$ , which tells that the volume of pre-training data is directly exchanged to the performance of fine-tuning tasks. Our empirical results suggest two strategies for reducing  $C$ : 1) Use bigger models and 2) fill the domain gap in terms of the decision rule and image distribution. For the latter, existing techniques such as domain randomization [55] would be helpful.

### 6.3 Limitations of this study

- In the experiments, the scale of data is relatively limited (million-scale, not billion).
- Although there are various visual tasks, our study only covers a few of them. Extending our observations to other visual tasks such as depth estimation, instance segmentation, keypoint detection, and other data domains such as language is future work.
- We only examined ResNet as a network architecture (no Transformers).
- The theoretical results assume several conditions that may contradict the actual setting in the experiments. For example, our theory relies on ASGD instead of vanilla SGD. Also, the optimal weights after fine-tuning are assumed to be close to the pre-training solution, which is not necessarily satisfied in the actual transfer learning setting.

### 6.4 Potential negative societal impact

Regarding synthetic-to-real transfer learning, a potential negative impact would be a data bias induced from synthetic images. Due to the reality gap, pre-trained models with synthetic images might contain a specific bias that would incur unexpected outcomes when applying to real-world applications. Detecting such bias and preventing negative consequences are both important future work.

Another possible concern is the amount of computation used for pre-training. While using synthetic images save data collection and annotation cost, they instead require computational power for data generation. Pre-training itself also uses a huge CPU/GPU power (see Section 3.2). The reduction of these computations and energies is a key challenge to keep our environment sustainable.

## Acknowledgments and Disclosure of Funding

We thank Daisuke Okanohara, Shoichiro Yamaguchi, Takeru Miyato, Masanori Koyama, Katsuhiko Ishiguro for valuable comments and discussions in the early stage of this study. We also thank Kenta Oono for reading the draft and providing detailed feedback. TS was partially supported by JSPS KAKENHI (18H03201, and 20H00576), Japan Digital Design and JST CREST. KF was partially supported by JST CREST JPMJCR2015.

## References

- [1] Z. Allen-Zhu, Y. Li, and Y. Liang. Learning and generalization in overparameterized neural networks, going beyond two layers. *CoRR*, abs/1811.04918, 2018. URL <http://arxiv.org/abs/1811.04918>.
- [2] S.-i. Amari, N. Fujita, and S. Shinomoto. Four types of learning curves. *Neural Computation*, 4(4):605–618, 1992.
- [3] S. Arora, S. Du, W. Hu, Z. Li, and R. Wang. Fine-grained analysis of optimization and generalization for overparameterized two-layer neural networks. In *Proceedings of the 36th International Conference on Machine Learning*, volume 97, pages 322–332, 2019.
- [4] Y. Bahri, E. Dyer, J. Kaplan, J. Lee, and U. Sharma. Explaining neural scaling laws. *arXiv preprint arXiv:2102.06701*, 2021.
- [5] P. L. Bartlett, D. J. Foster, and M. J. Telgarsky. Spectrally-normalized margin bounds for neural networks. In *Advances in Neural Information Processing Systems*, volume 30. Curran Associates, Inc., 2017.
- [6] J. Baxter. A model of inductive bias learning. *Journal of artificial intelligence research*, 12: 149–198, 2000.
- [7] D. Bolya, C. Zhou, F. Xiao, and Y. J. Lee. Yolact: Real-time instance segmentation. In *Proceedings of the IEEE/CVF International Conference on Computer Vision*, pages 9157–9166, 2019.

- [8] J. Borrego, A. Dehban, R. Figueiredo, P. Moreno, A. Bernardino, and J. Santos-Victor. Applying domain randomization to synthetic data for object category detection. *arXiv preprint arXiv:1807.09834*, 2018.
- [9] A. Caponnetto and E. De Vito. Optimal rates for regularized least-squares algorithm. *Foundations of Computational Mathematics*, 7(3):331–368, 2007.
- [10] L.-C. Chen, G. Papandreou, F. Schroff, and H. Adam. Rethinking atrous convolution for semantic image segmentation. *arXiv preprint arXiv:1706.05587*, 2017.
- [11] W. Chen, Z. Yu, S. D. Mello, S. Liu, J. M. Alvarez, Z. Wang, and A. Anandkumar. Contrastive syn-to-real generalization. *arXiv preprint arXiv:2104.02290*, 2021.
- [12] M. Denninger, M. Sundermeyer, D. Winkelbauer, Y. Zidan, D. Olefir, M. Elbadrawy, A. Lodhi, and H. Katam. Blenderproc. *arXiv preprint arXiv:1911.01911*, 2019.
- [13] J. Devaranjan, A. Kar, and S. Fidler. Meta-sim2: Unsupervised learning of scene structure for synthetic data generation. In *European Conference on Computer Vision*, pages 715–733. Springer, 2020.
- [14] S. Du, J. Lee, H. Li, L. Wang, and X. Zhai. Gradient Descent Finds Global Minima of Deep Neural Networks. In *Proceedings of the 36th International Conference on Machine Learning*, volume 97, pages 1675–1685, 2019.
- [15] S. S. Du, W. Hu, S. M. Kakade, J. D. Lee, and Q. Lei. Few-shot learning via learning the representation, provably. *arXiv preprint arXiv:2002.09434*, 2020.
- [16] R. Geirhos, P. Rubisch, C. Michaelis, M. Bethge, F. A. Wichmann, and W. Brendel. Imagenet-trained cnns are biased towards texture; increasing shape bias improves accuracy and robustness. *arXiv preprint arXiv:1811.12231*, 2018.
- [17] R. Geirhos, J.-H. Jacobsen, C. Michaelis, R. Zemel, W. Brendel, M. Bethge, and F. A. Wichmann. Shortcut learning in deep neural networks. *Nature Machine Intelligence*, 2(11):665–673, 2020.
- [18] G. Georgakis, A. Mousavian, A. C. Berg, and J. Kosecka. Synthesizing training data for object detection in indoor scenes. *arXiv preprint arXiv:1702.07836*, 2017.
- [19] P. Goyal, P. Dollár, R. Girshick, P. Noordhuis, L. Wesolowski, A. Kyrola, A. Tulloch, Y. Jia, and K. He. Accurate, large minibatch SGD: Training ImageNet in 1 hour. *arXiv preprint arXiv:1706.02677*, 2017.
- [20] K. He, R. Girshick, and P. Dollár. Rethinking imagenet pre-training. *arXiv preprint arXiv:1811.08883*, 2018.
- [21] T. Henighan, J. Kaplan, M. Katz, M. Chen, C. Hesse, J. Jackson, H. Jun, T. B. Brown, P. Dhariwal, S. Gray, C. Hallacy, B. Mann, A. Radford, A. Ramesh, N. Ryder, D. M. Ziegler, J. Schulman, D. Amodei, and S. McCandlish. Scaling laws for autoregressive generative modeling. *arXiv preprint arXiv:2010.14701*, 2020.
- [22] K. L. Hermann, T. Chen, and S. Kornblith. The origins and prevalence of texture bias in convolutional neural networks. *arXiv preprint arXiv:1911.09071*, 2019.
- [23] D. Hernandez, J. Kaplan, T. Henighan, and S. McCandlish. Scaling laws for transfer. *arXiv preprint arXiv:2102.01293*, 2021.
- [24] J. Hestness, S. Narang, N. Ardalani, G. Diamos, H. Jun, H. Kianinejad, M. M. A. Patwary, Y. Yang, and Y. Zhou. Deep learning scaling is predictable, empirically. *arXiv preprint arXiv:1712.00409*, 2017.
- [25] S. Hinterstoisser, O. Pauly, H. Heibel, M. Marek, and M. Bokeloh. An annotation saved is an annotation earned: Using fully synthetic training for object instance detection. *arXiv preprint arXiv:1902.09967*, 2019.

- [26] T. Hodaň, V. Vineet, R. Gal, E. Shalev, J. Hanzelka, T. Connell, P. Urbina, S. N. Sinha, and B. Guenter. Photorealistic image synthesis for object instance detection. In *2019 IEEE International Conference on Image Processing (ICIP)*, pages 66–70. IEEE, 2019.
- [27] T. Hodaň, M. Sundermeyer, B. Drost, Y. Labbé, E. Brachmann, F. Michel, C. Rother, and J. Matas. BOP challenge 2020 on 6D object localization. *European Conference on Computer Vision Workshops (ECCVW)*, 2020.
- [28] M. Huh, P. Agrawal, and A. A. Efros. What makes imagenet good for transfer learning? *arXiv preprint arXiv:1608.08614*, 2016.
- [29] M. Hutter. Learning curve theory. *arXiv preprint arXiv:2102.04074*, 2021.
- [30] A. Jacot, F. Gabriel, and C. Hongler. Neural tangent kernel: Convergence and generalization in neural networks. In *Advances in Neural Information Processing Systems 31*, pages 8571–8580. Curran Associates, Inc., 2018.
- [31] J. Kaplan, S. McCandlish, T. Henighan, T. B. Brown, B. Chess, R. Child, S. Gray, A. Radford, J. Wu, and D. Amodei. Scaling laws for neural language models. *arXiv preprint arXiv:2001.08361*, 2020.
- [32] A. Kolesnikov, L. Beyer, X. Zhai, J. Puigcerver, J. Yung, S. Gelly, and N. Houlsby. Big transfer (bit): General visual representation learning. *arXiv preprint arXiv:1912.11370*, 2019.
- [33] S. Kornblith, J. Shlens, and Q. V. Le. Do better imagenet models transfer better? *arXiv preprint arXiv:1805.08974*, 2018.
- [34] T.-Y. Lin, M. Maire, S. Belongie, J. Hays, P. Perona, D. Ramanan, P. Dollár, and C. L. Zitnick. Microsoft coco: Common objects in context. In *European conference on computer vision*, pages 740–755. Springer, 2014.
- [35] T.-Y. Lin, P. Dollár, R. Girshick, K. He, B. Hariharan, and S. Belongie. Feature pyramid networks for object detection. In *Proceedings of the IEEE conference on computer vision and pattern recognition*, pages 2117–2125, 2017.
- [36] J. Long, E. Shelhamer, and T. Darrell. Fully convolutional networks for semantic segmentation. In *Proceedings of the IEEE conference on computer vision and pattern recognition*, pages 3431–3440, 2015.
- [37] T. Mensink, J. Uijlings, A. Kuznetsova, M. Gygli, and V. Ferrari. Factors of influence for transfer learning across diverse appearance domains and task types. *arXiv preprint arXiv:2103.13318*, 2021.
- [38] M. Mohri, A. Rostamizadeh, and A. Talwalkar. *Foundations of machine learning*. MIT press, 2018.
- [39] M. Mousavi, A. Khanal, and R. Estrada. Ai playground: Unreal engine-based data ablation tool for deep learning. In *International Symposium on Visual Computing*, pages 518–532. Springer, 2020.
- [40] Y. Movshovitz-Attias, T. Kanade, and Y. Sheikh. How useful is photo-realistic rendering for visual learning? *arXiv preprint arXiv:1603.08152*, 2016.
- [41] A. Newell and J. Deng. How useful is self-supervised pretraining for visual tasks? *arXiv preprint arXiv:2003.14323*, 2020.
- [42] B. Neyshabur, R. Tomioka, and N. Srebro. Norm-based capacity control in neural networks. In *Proceedings of The 28th Conference on Learning Theory*, pages 1376–1401, 2015.
- [43] B. Neyshabur, S. Bhojanapalli, D. McAllester, and N. Srebro. Exploring Generalization in Deep Learning. In *Advances in Neural Information Processing Systems 30*, pages 5947–5956, 2017.
- [44] C. V. Nguyen, T. Hassner, M. Seeger, and C. Archambeau. LEEP: A new measure to evaluate transferability of learned representations. *arXiv preprint arXiv:2002.12462*, 2020.



- [45] A. Nitanda and T. Suzuki. Optimal rates for averaged stochastic gradient descent under neural tangent kernel regime. In *International Conference on Learning Representations*, 2021.
- [46] A. Nitanda, G. Chinot, and T. Suzuki. Gradient descent can learn less over-parameterized two-layer neural networks on classification problems, 2020.
- [47] S. Ren, K. He, R. Girshick, and J. Sun. Faster r-cnn: Towards real-time object detection with region proposal networks. *IEEE transactions on pattern analysis and machine intelligence*, 39(6):1137–1149, 2016.
- [48] J. S. Rosenfeld, A. Rosenfeld, Y. Belinkov, and N. Shavit. A constructive prediction of the generalization error across scales. *arXiv preprint arXiv:1909.12673*, 2019.
- [49] O. Russakovsky, J. Deng, H. Su, J. Krause, S. Satheesh, S. Ma, Z. Huang, A. Karpathy, A. Khosla, M. Bernstein, A. C. Berg, and L. Fei-Fei. ImageNet Large Scale Visual Recognition Challenge. *International Journal of Computer Vision (IJCV)*, 115(3):211–252, 2015. doi: 10.1007/s11263-015-0816-y.
- [50] U. Sharma and J. Kaplan. A neural scaling law from the dimension of the data manifold. *arXiv preprint arXiv:2004.10802*, 2020.
- [51] H. Su, C. R. Qi, Y. Li, and L. J. Guibas. Render for cnn: Viewpoint estimation in images using cnns trained with rendered 3d model views. In *Proceedings of the IEEE International Conference on Computer Vision*, pages 2686–2694, 2015.
- [52] C. Sun, A. Shrivastava, S. Singh, and A. Gupta. Revisiting unreasonable effectiveness of data in deep learning era. In *Proceedings of the IEEE international conference on computer vision*, pages 843–852, 2017.
- [53] T. Suzuki. Fast generalization error bound of deep learning from a kernel perspective. In *Proceedings of the Twenty-First International Conference on Artificial Intelligence and Statistics*, volume 84, pages 1397–1406, 2018.
- [54] Y. Tian, Y. Wang, D. Krishnan, J. B. Tenenbaum, and P. Isola. Rethinking few-shot image classification: a good embedding is all you need? *arXiv preprint arXiv:2003.11539*, 2020.
- [55] J. Tobin, R. Fong, A. Ray, J. Schneider, W. Zaremba, and P. Abbeel. Domain randomization for transferring deep neural networks from simulation to the real world. *arXiv preprint arXiv:1703.06907*, 2017.
- [56] J. Tremblay, A. Prakash, D. Acuna, M. Brophy, V. Jampani, C. Anil, T. To, E. Cameracci, S. Bochoon, and S. Birchfield. Training deep networks with synthetic data: Bridging the reality gap by domain randomization. *arXiv preprint arXiv:1804.06516*, 2018.
- [57] N. Tripurani, M. I. Jordan, and C. Jin. On the theory of transfer learning: The importance of task diversity. *arXiv preprint arXiv:2006.11650*, 2020.
- [58] C. Wei and T. Ma. Improved Sample Complexities for Deep Neural Networks and Robust Classification via an All-Layer Margin. In *International Conference on Learning Representations*, 2020. URL [https://openreview.net/forum?id=HJe\\_yR4Fwr](https://openreview.net/forum?id=HJe_yR4Fwr).
- [59] A. Zamir, A. Sax, W. Shen, L. Guibas, J. Malik, and S. Savarese. Taskonomy: Disentangling task transfer learning. *arXiv preprint arXiv:1804.08328*, 2018.
- [60] B. Zhou, H. Zhao, X. Puig, T. Xiao, S. Fidler, A. Barriuso, and A. Torralba. Semantic understanding of scenes through the ade20k dataset. *arXiv preprint arXiv:1608.05442*, 2016.
- [61] B. Zhou, H. Zhao, X. Puig, S. Fidler, A. Barriuso, and A. Torralba. Scene parsing through ade20k dataset. In *Proceedings of the IEEE conference on computer vision and pattern recognition*, pages 633–641, 2017.
- [62] B. Zoph, G. Ghiasi, T.-Y. Lin, Y. Cui, H. Liu, E. D. Cubuk, and Q. V. Le. Rethinking pre-training and self-training. *arXiv preprint arXiv:2006.06882*, 2020.

# Supplementary Material

## A Training Details

### A.1 Object detection

We used Faster-RCNN [47] with FPN [35] as object detection models and ResNet [19] as a backbone network of Faster-RCNN.

We used the following training procedure: We trained the model using momentum SGD of momentum 0.9 with weight decay of  $10^{-4}$ . The global batch size was set to 64 when training ResNet18, ResNet34, ResNet50, and ResNet101. The batch size was set to 32 when training ResNet152 to avoid out-of-memory errors. The batch statistics in batch normalization layers were computed across all GPUs. We used a base image size of  $640 \times 640$  in the same way as YOLACT training [7]. We used mixed16 training to reduce the memory footprint. We also adopted random horizontal flipping as data augmentation to images. The learning rate was set to 0.02, and we used the cosine decay with a warmup scheme. The warmup length is 120,000 images (3,750 iterations for ResNet152 and 1,875 iterations for other models). As for evaluation, we followed the standard settings in COCO dataset [47].

We pre-trained the model with 14,400,000 images (450,000 iterations for ResNet152 and 225,000 iterations for other models). We used the models that achieved the best mAP as the initial value of fine-tuning.

We used COCO [34] as the fine-tuning dataset. We trained the model with 1,440,000 images (45,000 iterations for ResNet152 and 22,500 iterations for other models) during fine-tuning.

### A.2 Semantic segmentation

We used DeepLabV3 [10] with the softmax cross-entropy loss as the semantic segmentation model and ResNet50 [19] as its backbone. The model configuration follows the implementation in torchvision<sup>5</sup>. It should be noted that DeepLabV3 requires *dilated* ResNet as the backbone, which is not the case in object detection and classification tasks. Even though, the shapes of weight tensors of dilated ResNet50 exactly match those of non-dilated ResNet50; thus we can use the pre-trained weights of dilated and non-dilated ResNet50 interchangeably.

The learning procedure is based on the reference implementation<sup>6</sup> of torchvision. We added an auxiliary branch based on FCN [36] which takes conv4 of the backbone as the input. In the computation of loss function, the loss for the auxiliary branch is computed in the same way as for the main branch and is added to the overall loss after multiplying by the factor 0.5. The model was trained using momentum SGD of momentum 0.9 with weight decay of  $10^{-4}$ . The global batch size was set to 32. The batch statistics in batch normalization layers were computed across all GPUs. During training, images were first resized so that the length of the shorter edge becomes an integer uniformly chosen from  $[520 \times 0.5, 520 \times 2]$ , then horizontally flipped with probability 0.5, finally randomly cropped to  $480 \times 480$ . The learning rate (LR) was decayed according to the polynomial LR schedule of rate 0.9 and initial LR of 0.02. For the parameters of the auxiliary classifier, the LR was multiplied by 10. The evaluation was performed once every 3,125 iterations (almost equivalent to 5 epochs in full ADE20K). In the evaluation, images were resized so that the length of the shorter edge becomes 520.

In pre-training, we trained 125,000 iterations which roughly equals 200 epochs in full ADE20K [61]. We used the model that achieved the best mIoU as the initial value of fine-tuning. We pre-trained models using our synthetic datasets. When training with them, backgrounds (points at which no foreground objects were present) were also considered to be a separate class in semantic segmentation.

We used the ADE20K [61] datasets as the fine-tuning target. In fine-tuning, we trained the model for 18,750 iterations, which correspond to 30 epochs of full ADE20K. The metric was mIoU score.

---

<sup>5</sup><https://github.com/pytorch/vision>

<sup>6</sup><https://github.com/pytorch/vision/tree/master/references/segmentation>

### A.3 Multi-label classification

We used ResNet [19] with binary cross-entropy used as the loss function in multi-label classification. We used the following training procedure: We trained the model using momentum SGD of momentum 0.9 with weight decay of  $10^{-4}$ . The batch size was set as 32 per GPU, thus 256 in total. We trained the models for 112,500 iterations. The input size of the images was simply resized to  $640 \times 640$ . We adopted random horizontal flipping as data augmentation to images. The learning rate was set to 0.1. The cosine decay with a warmup scheme was used. The warmup length was 120,000 images. The evaluation was performed once every 120,000 images. In the evaluation, the image size was the same as that used during training, and data augmentation was not used. We used the mAP score as the metric.

### A.4 Single-label classification

As in multi-label classification, we used ResNet. The softmax cross-entropy was used as the loss function of the single-label classification. The learning procedure is based on [19]. However, we used cosine decay for the learning rate scheduling.

### A.5 Surface normal estimation

As in semantic segmentation, we used DeepLabV3 [10] as the model for surface normal estimation. The model configuration and the training procedure were exactly the same as in semantic segmentation, except for the following changes:

- Dimension of output channels was changed to 3, each of which corresponds to the 3 axes of the normal vector,
- Initial LR was changed to 0.04,
- Length of pre-training was 200,000 iterations, which corresponds to 100 epochs in our synthetic dataset,
- Random flipping was not performed during the data augmentation, and
- Loss function was the average of the value,  $1.0 - \mathbf{n} \cdot \hat{\mathbf{n}}$ , which was computed for each valid pixel where  $\mathbf{n}$  is the ground-truth normal vector and  $\hat{\mathbf{n}}$  is the model output (after L2 normalization).

## B Synthetic Data Details

The data generation strategy is based on the “on surface sampling” setting in the BoP challenge dataset<sup>7</sup>. In this setting, the sampled objects will be spawned in a cube-shaped room with one point light and one surface light. As the objects to be spawn, we used all the BoP object sets, i.e., LM, T-LESS, ITODD, HB, YCB-V, RU-APC, IC-BIN, IC-MI, TUD-L, and TYO-L.<sup>8</sup> There are 173 objects in total. After generated a random scene (position of objects, lights, etc), we took 10 pictures by 10 different camera poses. This means that, if we have 10K images in total, there are 1K unique scenes, and 9K images are inflated by just changing the camera angle and position.

To control the data complexity, we selected four attributes in the generation strategy and prepared two options for each.

*Appearance* controls how many objects are generated in a room in a single scene. For each scene, we randomly select ten objects for the **multiple** setting and one object for the **single** setting.

*Light* controls the light sources. In the **random** setting, the color, height, and strength of lights are randomized. In contrast, in the **fix** setting, they are all fixed.

*Background* controls the texture of the room, i.e., floor and walls. In the **random** setting, we assign a random PBR material from the CC0 Textures<sup>9</sup> library, and we selected one carpet texture for the **fix** setting.

---

<sup>7</sup>[https://github.com/DLR-RM/BlenderProc/tree/main/examples/bop\\_challenge](https://github.com/DLR-RM/BlenderProc/tree/main/examples/bop_challenge)

<sup>8</sup><https://bop.felk.cvut.cz/datasets/>

<sup>9</sup><https://ambientcg.com>

*Object texture* controls the object set to be used. The BoP object set consists of several types of object sets as described above. Among them, T-LESS and ITODD consist of industry-relevant objects and they do not have textures and colors.<sup>10</sup> For the **w/o** setting, we only used such texture-less objects to be sampled. In contrast, we sample all the 173 objects include T-LESS and ITODD in the **w/** setting.

We generated eight variations of datasets by changing these attributes, which were used in the experiments of Section 4.4. Figure 6 shows the example of generated images with the value of each attribute.

## C Additional Experiments

### C.1 Estimated parameters in the cross-task setting

Figure 7 shows the estimated parameters ( $\alpha, C$ ) at the experiments described in Section 4.1. Note that the result of  $\alpha$  at `normal→semseg` is omitted because its estimated value is highly unstable (the standard deviation is larger than 1).

### C.2 Experiments with million synthetic images

We examined the scaling behavior with more pre-training images. In addition to 64 thousand images (64K) used in the previous experiments, we generated another data set that contained 1.28 million examples (1.28M). We pre-trained the models with the data set and fine-tuned them by following the same protocol of the previous experiments. The results (Figure 8) show that the empirical results are straightforwardly extended from the previous results (Figure 3) in the `objdet→objdet` case. In the `mulclass→sinclass` case, we see small “bumps” around  $10^{4.5}$  of x-axis where the numbers of images used for pre-training were overlapped in the 64K and 1.28M data sets. We suspect that these bumps occurred because the density of synthetic scenes was different. As mentioned in Section B, the ratio of unique scenes in the entire data sets is  $1/10$ . In pre-training, we randomly shuffled and subsampled the examples from each data set. The subsampling process, however, could change the ratio of unique scenes. For example, the sample sizes of 64K and 5% subsamples of 1.28M are equal, but the ratios of unique scenes are  $1/10 = 0.1$  for the former and  $\sim 0.8$  in expectation for the latter. Namely, 5% of 1.28M contains unique scenes 8 times more than 100% of 64K. Clearly, having more unique scenes works positively for pre-training, and it would fill the performance gap to some extent.

### C.3 Linearized results

The transfer gap  $C$  in (1) causes a plateau of the scaling law. Conversely, if we subtract the estimated  $C$  from the results, we must be able to recover the power-law scaling. To confirm this, we subtracted the estimated  $C$  from the empirical errors  $\hat{L}$  of the previous results. Figures 9–11 show the modified version of scaling law fittings. Overall, the empirical errors behave linearly along with the estimated power-law term  $Dn^{-\alpha}$ . Note that, in `mulclass→semseg` and `normal→semseg`, a few points of  $\hat{L}$  become negative after subtracting  $C$ , and these points are not depicted.

## D Empirical dependency between $\alpha$ and $D$

When  $C$  is non-zero, the joint estimation of  $D$  and  $\alpha$  in (1) have an issue of numerical stability due to the small number of observations and noise, which can cause high dependence on each other. Figure 12 (left) shows the curves of (1) with  $C = 0.5$ , where the solid red curve is  $D = 0.5, \alpha = 0.4$  and the dashed blue line is  $D = 1, \alpha = 0.5$ . We see that both curves are almost indistinguishable for a large  $n$ . Figure 12 (right) shows the actual landscape in terms of  $\alpha$  and  $D$  of the nonlinear least-squares at `objdet→objdet`, the bright areas indicate the fitting loss is small. We see that there is a quadratic-like trajectory in the landscape, which implies the solutions are somehow redundant. Similar landscapes were observed for other tasks (Figure 13).

To avoid this issue, we fixed a common  $D$  for all the cases and estimated  $\alpha$  for each. To determine  $D$ , we used the following procedure. First, we prepared two global parameters  $\hat{\alpha}, \hat{D}$  and set 0.5 as

<sup>10</sup>T-Less and ITODD contain 30 and 28 objects, respectively.



Figure 6: Example of generated datasets

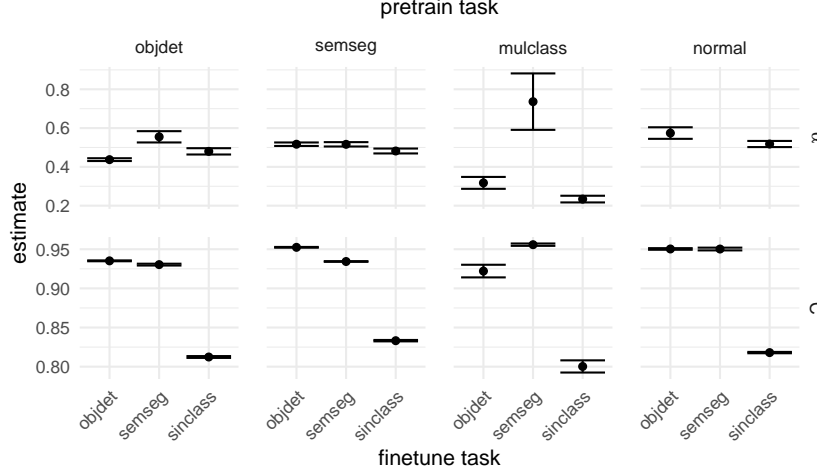


Figure 7: The estimated values of the pre-training rate  $\alpha$  and the transfer gap  $C$  in the cross-task setting (as the same as Figure 1). The error bars present the standard error of the estimates in the least squares.

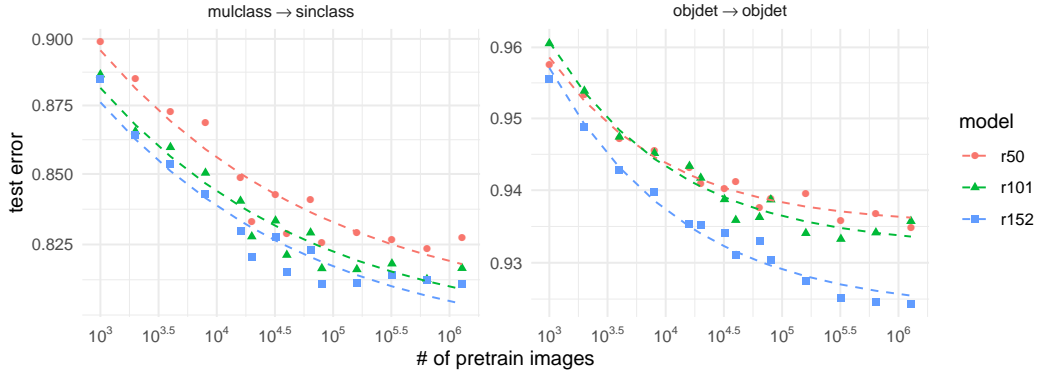


Figure 8: Empirical results and fitted scaling curve with million-scale pre-training.

their initial values. Then, we fitted the curves by two equations,  $Dn^{-\hat{\alpha}} + C$  and  $\hat{D}n^{-\alpha} + C$ , and estimated  $\alpha$  and  $D$ . Next, we computed the median of  $\alpha$  and substituted them into  $\hat{\alpha}$ . We did the same for  $D$  and  $\hat{D}$ . After a few iterations, we got a converged value of  $\hat{D} = 0.48$ . In the experiments, we used the value for  $D$  and fixed it.

## E Details of Theoretical Analysis

This section gives details of the theoretical discussions given in Section 5. For the analysis of learning and generalization bound, we use the techniques developed recently by Nitanda and Suzuki [45]. There are many works on the generalization of neural networks. To list a few, Neyshabur et al. [42], Neyshabur et al. [43], Bartlett et al. [5], Wei and Ma [58], and Suzuki [53] analyze the generalization of neural networks based on complexity bounds. These generalization bounds, however, do not consider an algorithm of learning, such as stochastic gradient descent (SGD). Recently, learning dynamics of neural networks has been analyzed based on Neural Tangent Kernel (NTK) [30] and global convergence of wide neural networks has been revealed [1, 14]. Based on the NTK framework, Arora et al. [3] and Nitanda et al. [46] showed a generalization bound of the gradient descent learning of neural networks. More recently, Nitanda and Suzuki [45] focused the functional space given by NTK and showed that the two-layer neural network with averaged SGD achieves the minimax optimal rate with respect to the function class used in the standard theory of function estimation with kernels.

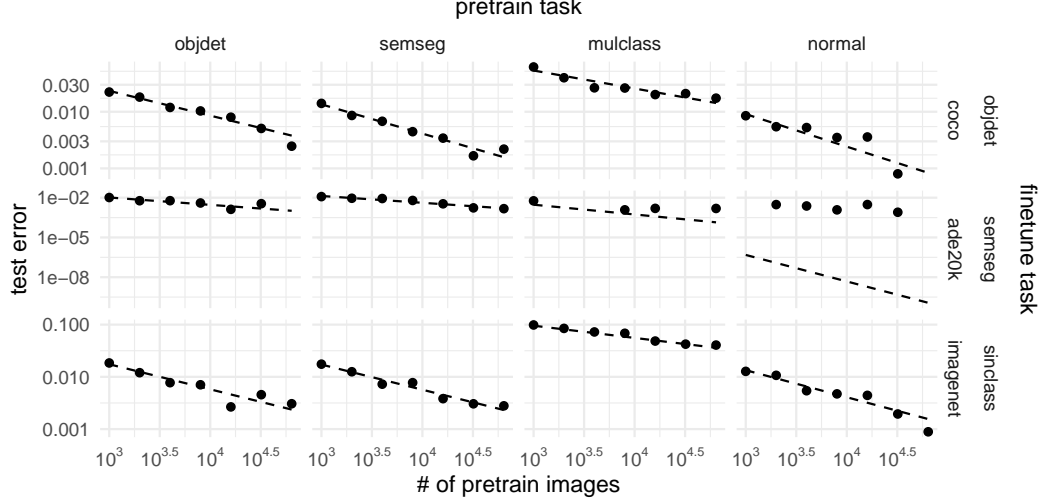


Figure 9: The linearized version of Figure 1.

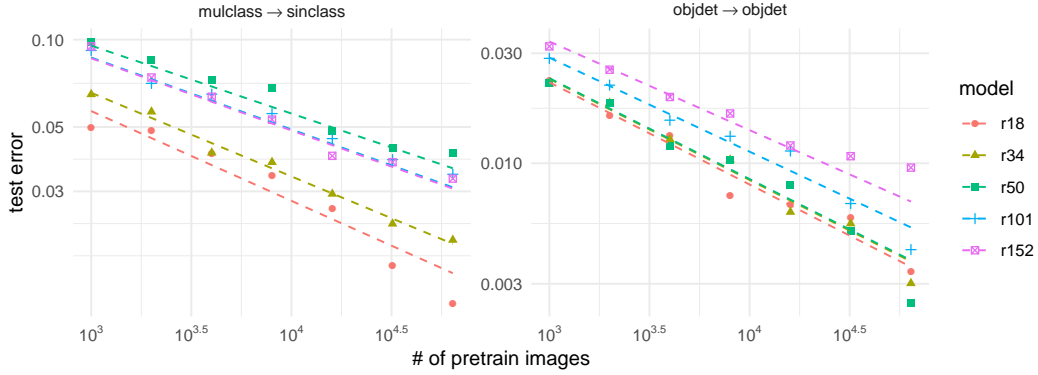


Figure 10: The linearized version of Figure 3.

We employ the method of Nitanda and Suzuki [45], which is the most suitable for our analysis of transfer learning: it enables to examine the dependence on the initial parameter in the learning, and avoid the assumption of a positive margin of eigenvalues used in [3, 46].

### E.1 Problem Setting

In the pre-training, the task is to learn the target function  $\varphi_0$  with  $T_0$  training data  $(\tilde{x}_i, \tilde{y}_i)_{i=1}^{T_0}$ , where  $y_i = \varphi_0(x_i)$ , while in the fine-tuning phase, the network is initialized by the final parameter learned by the pre-training, and the whole parameter is updated in the training. We assume that the target function in the fine-tuning is given by

$$\varphi(x) = \varphi_0(x) + \varphi_1(x), \quad (10)$$

and  $T_1$  training data is given by  $(x_j, y_j)_{j=1}^{T_1}$  with  $y_j = \varphi(x_j)$ . Note that, for simplicity of analysis, we assume noiseless training data, i.e., we assume the supervised signal  $y_j$  is given by a deterministic function of  $x_j$ , but extension to more general cases is not difficult as discussed in [45]. In this setting, the goal of the fine-tune phase will be to learn the additional function  $\varphi_1$  mainly. In the analysis, the data are assumed to satisfy  $x \in \mathbb{R}^d$ ,  $\|x\|_2 = 1$  and  $y \in [0, 1]$ . The distribution of the input data  $x$  is denoted by  $\rho_X$ , and the same for the pre-training and fine-tune.



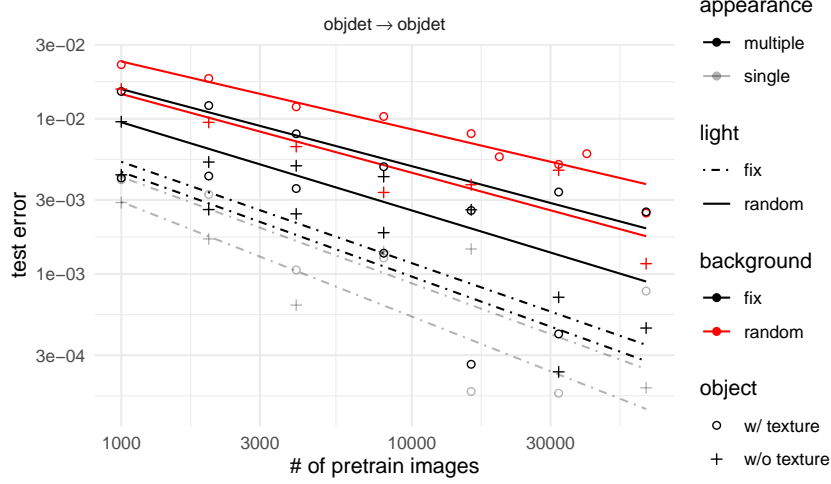


Figure 11: The linearized version of Figure 5.

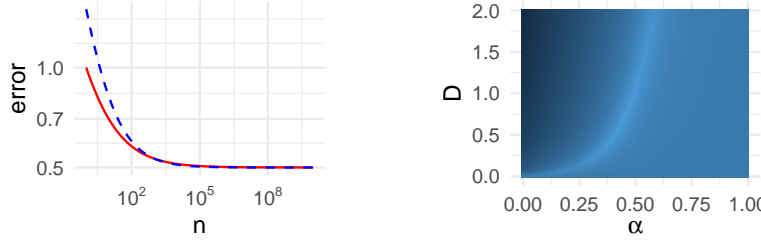


Figure 12: Examples of parameter dependency.

For tractable theoretical analysis, we consider a simple scalar-valued two-layer neural network model with  $M$  hidden units:

$$g_{\Theta}(x) = \frac{1}{\sqrt{M}} \sum_{r=1}^M a_r \sigma(b_r^T x). \quad (11)$$

We omit the bias term, but with obvious modification, it is not difficult to include it (see [45]).

As in [45], we consider the averaged stochastic gradient descent (ASGD), where one training sample is given at every time step for the stochastic gradient descent as in online learning, and all the parameters in the time course are averaged after the final time step for the inference, that is, after proceeding up to prescribed  $T$  ( $T = T_0$  or  $T_1$ ) time steps, the parameter to be used in the inference is given by

$$\bar{\Theta}^{(T)} := \frac{1}{T+1} \sum_{t=0}^T \alpha_t \Theta^{(t)}, \quad (12)$$

where  $\alpha_t$  is the weights for the average, and can be  $\alpha_t = 1$ . The final network uses this averaged parameter, i.e., the final network is given by  $g_{\bar{\Theta}^{(T)}}(x)$ .

The parameter is initialized as  $\Theta^{(0)} = (a_1^{(0)}, b_1^{(0)}, \dots, a_M^{(0)}, b_M^{(0)})$ . For the pre-training, each  $b^{(0)}$  is independently given by the uniform distribution on the unit sphere. As in [45],  $a^{(0)}$  are initialized as 1 or  $-1$  so that  $g_{\Theta^{(0)}} = 0$ . As explained before, the initial parameter of the fine-tune is the same as the averaged parameter of the pre-training  $\bar{\Theta}_{pre}^{(T_0)}$ . The objective function to minimize for the pre-train and fine-tune is given by the following regularized empirical risk:

$$L(\Theta) := \frac{1}{2} \sum_i (y_i - g_{\Theta}(x_i))^2 + \frac{\lambda}{2} \left\{ \|a - a^{(0)}\|_2^2 + \sum_r \|b_r - b_r^{(0)}\|_2^2 \right\}, \quad (13)$$

where  $\lambda$  is the regularization coefficient, which is a hyperparameter. The values of  $\lambda$  in the pre-train and fine-tune can be different, and denoted by  $\lambda_0$  and  $\lambda_1$ , respectively.



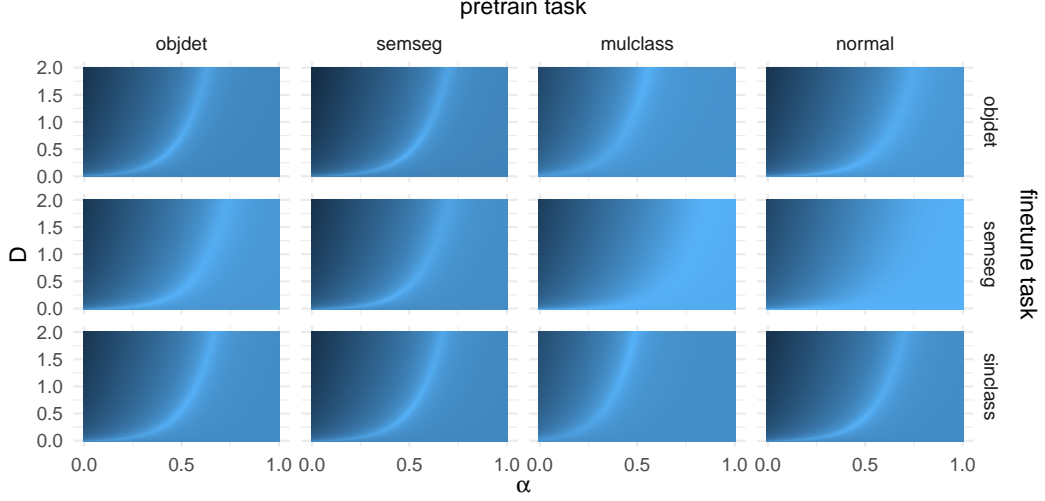


Figure 13: Loss landscapes of curve fittings.

At time step  $t$  ( $t \leq T - 1$ ), one datum  $x_i$  is sampled from  $\rho_X$  independently, and  $(x_i, y_i)$  (or  $(\tilde{x}_i, \tilde{y}_i)$  in pre-training) is used to update the parameter according to the rule:

$$\Theta^{(t+1)} = \Theta^{(t)} - \eta \frac{\partial L(\Theta^{(t)})}{\partial \Theta}, \quad (14)$$

where  $\eta$  is a learning rate. More explicitly,

$$\begin{aligned} a_r^{(t+1)} - a_r^{(0)} &= (1 - \eta\lambda)(a_r^{(t)} - a_r^{(0)}) - \frac{\eta}{\sqrt{M}}(g_{\Theta^{(t)}} - y_t)\sigma(b_t^{(t)T}x_t), \\ b_r^{(t+1)} - b_r^{(0)} &= (1 - \eta\lambda)(b_r^{(t)} - b_r^{(0)}) - \frac{\eta}{\sqrt{M}}(g_{\Theta^{(t)}} - y_t)a_r\sigma'(b_t^{(t)T}x_t)x_t. \end{aligned} \quad (15)$$

## E.2 Neural Tangent Kernel

In the theoretical analysis, the neural tangent kernel (NTK) [30] is used for approximating the dynamics of ASGD by a linear functional recursion on the corresponding function space. The NTK of this model is given by

$$k_\infty(x, x') = E_{b^{(0)}}[\sigma(b^{(0)T}x)\sigma(b^{(0)T}x')] + x^T x' E_{b^{(0)}}[\sigma'(b^{(0)T}x)\sigma'(b^{(0)T}x')]. \quad (16)$$

The positive definite kernel  $k_\infty$  naturally defines a reproducing kernel Hilbert space (RKHS), which is denoted by  $\mathcal{H}_\infty$ .

The integral operator  $\Sigma_\infty$  on  $L^2(\rho_X)$  is defined by

$$\Sigma_\infty f := \int k_\infty(\cdot, x)f(x)d\rho_X(x). \quad (17)$$

It is known that  $\Sigma_\infty$  admits eigendecomposition

$$\Sigma_\infty \phi_s = \gamma_s \phi_s, \quad (18)$$

where  $\gamma_1 \geq \gamma_2 \geq \dots > 0$  are eigenvalues in descending order. Mercer's theorem tells that  $k_\infty$  has an expansion:

$$k_\infty(x, x') = \sum_{s=1}^{\infty} \gamma_s \phi_s(x)\phi_s(x'),$$

where the convergence is understood as in  $L^2(\rho_X)$  for general, and absolutely and uniformly if  $\rho_X$  is a uniform distribution on a compact set.

### E.3 Assumptions

For theoretical analysis, we make the following assumptions. For an operator  $\Sigma$ , the range of  $\Sigma$  is denoted by  $\mathcal{R}(\Sigma)$ .

- (A1)  $\sigma$  is differentiable up to the second order, and there exists  $C > 0$  such that  $\|\sigma''\|_\infty \leq C$ ,  $\|\sigma'\|_\infty \leq 2$ , and  $|\sigma(u)| \leq 1 + |u|$  for  $\forall u \in \mathbb{R}$ .
- (A2)  $\text{supp}(\rho_X) \subset \{x \in \mathbb{R}^d \mid \|x\| \leq 1\}$  and  $y \in [-1, 1]$ .
- (A3) There exist  $1/2 \leq r_0, r_1 \leq 1$  such that  $\varphi_0 \in \mathcal{R}(\Sigma_\infty^{r_0})$  and  $\varphi_1 \in \mathcal{R}(\Sigma_\infty^{r_1})$ .
- (A4) There exists  $\xi > 1$  such that  $\gamma_\ell = \Theta(\ell^{-\xi})$ .

As in (A1), we assume that the activation  $\sigma$  is differentiable in this paper. In [45], however, they have developed a theory on how to extend the result to the case of ReLU by approximating it with a smooth function. It is well known that Assumption (A4) specifies the complexity of the hypothesis class  $\mathcal{H}_\infty$  [9]. The assumption (A3) controls the smoothness of the target functions  $\varphi_0, \varphi_1$ . In fact, the functions are included in  $\mathcal{H}_\infty$  since  $r_i \geq 1/2$ . When a function  $f$  has the expansion  $f = \sum_\ell a_\ell \phi_\ell$ , the assumption  $f \in \mathcal{R}(\Sigma_\infty^r)$  means  $a_\ell = o(\ell^{-\xi r - 1/2})$ . A function with a larger  $r$  is smoother, which is easier to learn. It is known [9, 45] that  $\xi$  and  $r$  are the two basic parameters to control the convergence rate of generalization for a large sample size. In the sequel, when  $\phi \in \mathcal{R}(\Sigma^r)$  and  $\phi = \Sigma^r \psi$ , we write  $\|\Sigma^{-r} \phi\| := \|\psi\|$ .

### E.4 Generalization bound

The pre-training can be discussed in the standard setting of [45]. Let  $\widehat{\varphi}_0$  be the result of pre-train, i.e.,  $\widehat{\varphi}_0 := g_{\overline{\Theta}_{pre}^{(T_0)}}$ , where  $\overline{\Theta}_{pre}^{(T_0)}$  is the averaged parameter by ASGD. By optimizing the regularization parameter  $\lambda_0$ , Corollary 1 in [45] shows that for sufficiently large  $M$ , with a choice of  $\lambda_0 = T_0^{-\xi/(2r_0\xi+1)}$ ,

$$E\|\widehat{\varphi}_0 - \varphi_0\|_{L^2(\rho_X)}^2 = \varepsilon_M + cT_0^{-\frac{2r_0\xi}{2r_0\xi+1}} (1 + \|\Sigma_\infty^{-r_0} \varphi_0\|_{L^2(\rho_X)}^2) \quad (19)$$

with high probability, where  $c$  is a universal constant and  $\varepsilon_M$  is arbitrarily small for a large  $M$ . It is known [9] that the rate  $T_0^{-\frac{2r_0\xi}{2r_0\xi+1}}$  achieves the minimax optimal rate with respect to  $T_0$  over the class specified by  $r_0$  and  $\xi$ .

In fine-tuning, the initial parameter is given by  $\Theta^{(0)} = \overline{\Theta}_{pre}^{(T_0)}$ , and ASGD is applied with  $(x_t, y_t)$  for  $t = 1, \dots, T_1$ .

By extending Theorem 1 in [45], we can derive a generalization bound in the following theorem. Recall that the regularization coefficient and learning coefficient of fine-tuning are denoted by  $\lambda_1$  and  $\eta_1$ , respectively.

**Theorem 2.** *Suppose Assumptions (A1)-(A3) hold. After pre-training that gives Eq. (6), fine-tune the network with a learning rate that satisfies  $4(6 + \lambda_1)\eta_1 \leq 1$ . Then, for any  $\varepsilon > 0$ ,  $\|\Sigma_\infty\|_{op} \geq \lambda_1 > 0$ ,  $\delta \in (0, 1)$ , and  $T_1 \in \mathbb{N}$ , there exists  $M_0 \in \mathbb{N}$  such that for any  $M \geq M_0$ , the following holds with high probability at least  $1 - \delta$  over the random initialization of pre-training:*

$$\begin{aligned} & E\|g_{\overline{\Theta}^{(T_1)}} - \varphi\|_{L^2(\rho_X)}^2 \\ & \leq \varepsilon + c_0 \lambda_1^{2r_0} \|\Sigma_\infty^{-r_0} \varphi_0\|_{L^2(\rho_X)}^2 + c_1 \lambda_1^{2r_1} \|\Sigma_\infty^{-r_1} \varphi_1\|_{L^2(\rho_X)}^2 \\ & \quad + \frac{c_2}{T_1 + 1} \{ \lambda_1^{-1} E\|\widehat{\varphi}_0 - \varphi_0\|_{L^2(\rho_X)}^2 (1 + \|\Sigma_\infty^{-r_0} \varphi_0\|_{L^2(\rho_X)}^2) + \lambda_1^{2r_1-1} \|\varphi_0\|_{L^2(\rho_X)}^2 + \|\varphi_1\|_{\mathcal{H}_\infty}^2 \} \\ & \quad + \frac{c_3}{(T_1 + 1)^2 \eta_1^2} \{ \lambda_1^{-2} E\|\widehat{\varphi}_0 - \varphi_0\|_{L^2(\rho_X)}^2 (1 + \|\Sigma_\infty^{-r_0} \varphi_0\|_{L^2(\rho_X)}^2) + \lambda_1^{2r_1-2} \|\varphi_0\|_{L^2(\rho_X)}^2 + \lambda_1^{-1} \|\varphi_1\|_{\mathcal{H}_\infty}^2 \} \\ & \quad + \frac{c_4}{T_1 + 1} (1 + \|\varphi\|_{\mathcal{H}_\infty}^2 + 24 \|\Sigma_\infty^{-r_0} \varphi\|_{L^2(\rho_X)}^2) \text{Tr}[\Sigma_\infty(\Sigma_\infty + \lambda_1 I)^{-1}], \end{aligned} \quad (20)$$

where  $\widehat{\varphi}_0$  is the result of pre-train and  $c_i$  ( $i = 0, 1, 2, 3, 4$ ) are universal constants.

The term  $\varepsilon$  is arbitrary small for a large value of  $M$ , i.e., wide network. The proof of Theorem 2 will be given in Section E.6.

## E.5 Analysis of convergence rates

We consider the rates of the generalization bound for  $E\|g_{\Theta(T_1)} - \varphi\|_{L^2(\rho_X)}^2$  with respect to  $T_1$ . As typical cases, we assume  $\lambda_1 \rightarrow 0$  and  $\eta_1 = O(1)$  as  $T_1 \rightarrow \infty$ . The dominant terms in Eq. (20) may vary according to the configurations of  $\lambda_1, \eta_1$  depending on  $T_1$ . We will show rates in some settings.

First, note that under Assumption (A4), the factor  $\text{tr}[\Sigma_\infty(\Sigma_\infty + \lambda_1 I)^{-1}]$  is given by [9]

$$\text{Tr}[\Sigma_\infty(\Sigma_\infty + \lambda_1 I)^{-1}] = O(\lambda_1^{-1/\xi}). \quad (21)$$

By neglecting  $\varepsilon$ , the terms in Eq. (20) thus have the following rates:

$$\begin{aligned} (a0) \lambda_1^{2r_0}, \quad (a1) \lambda_1^{2r_1}, \quad (b) T_1^{-1} \lambda_1^{-1} R_0, \quad (c) T_1^{-1} \lambda_1^{2r_1-1}, \quad (d) T_1^{-1}, \\ (e) T_1^{-2} \eta_1^{-2} \lambda_1^{-2} R_0, \quad (f) T_1^{-2} \eta_1^{-2} \lambda_1^{2r_1-2}, \quad (g) T_1^{-2} \eta_1^{-2} \lambda_1^{-1}, \quad (h) T_1^{-1} \lambda_1^{-1/\xi}. \end{aligned} \quad (22)$$

Here  $R_0 := E\|\hat{\varphi}_0 - \varphi_0\|_{L^2(\rho_X)}^2$  is regarded as a constant rate, but explicitly shown for the later use.

Since  $\lambda_1 \rightarrow 0$  and  $r_1 \geq 1/2$ , (c) and (d) are smaller than (b). Likewise, (f) and (g) are smaller than (e). The candidates of dominant terms are thus (a0), (a1), (b), (e), (g), and (h).

### E.5.1 Large regularization coefficient

In transfer learning, it is reasonable to use strong regularization in fine-tuning, which encourages the parameters to stay close to the initial value that is obtained in the pre-training. In this subsection, we consider the case where  $\lambda_1$  is larger than  $T_1^{-\frac{\xi}{2r_1\xi+1}}$ , which would be the optimal rate if the network was trained with random initialization (see [45]). If  $\lambda_1 = T_1^{-\frac{\xi}{2r_1\xi+1}}$  was taken, it is easy to see that the influence of pre-training would not appear explicitly in the rate. In the sequel, we write  $F \ll G(T_1)$  if there are  $a > 0$  and  $T^*$  such that  $F \leq aG(T_1)$  for all  $T_1 \geq T^*$ . In this notation, we assume

$$\lambda_1 \gg T_1^{-\frac{\xi}{2r_1\xi+1}}. \quad (23)$$

The rate  $\lambda_1 = T_1^{-\frac{\xi}{2r_1\xi+1}}$ , which is optimal in the standard training, is given by equating the rates of (a1) and (h). Therefore, under the assumption of Eq. (23), the rate (a1) is larger than (h), and thus it suffices to consider (a0), (a1), (b) and (e) as the candidates of dominant terms. Note that, if  $\lambda_1 \rightarrow 0$ , the terms (a0) and (a1) decrease, while (b) and (e) increase to infinity. We will discuss the possible cases of dominant terms under this assumption in the sequel. We introduce  $\zeta$  such that  $\eta_1 = T_1^{-\zeta}$ .

**(Case I)  $T_1 \lambda_1 \eta_1^2 \ll 1$ : Small learning rate.** In this case, (e)  $\gg$  (b). We equate (a0) or (a1) with (e) to obtain the optimal  $\eta_1$ .

**(I-A)  $r_0 \geq r_1$ .** Since  $\lambda_1 \rightarrow 0$  for  $T_1 \rightarrow \infty$ , (a1) is larger than (a0). By equating (a1) and (e), we have

$$\lambda_1 = T_1^{-\frac{1-\zeta}{r_1+1}} R_0^{\frac{1}{2r_1+2}}, \quad (24)$$

and the dominant rate of Eq. (22) is

$$T_1^{-\frac{2r_1(1-\zeta)}{r_1+1}} R_0^{\frac{r_1}{r_1+1}}. \quad (25)$$

The condition  $\lambda_1 \rightarrow 0$  is equivalent to  $\zeta < 1$ . There are two other conditions:  $\lambda_1 \gg T_1^{-\frac{\xi}{2r_1\xi+1}}$  and  $T_1 \lambda_1 \eta_1^2 \ll 1$ . Given  $R_0$  is of constant rate, the former is equivalent to  $-\frac{\xi}{2r_1+1} \leq -\frac{1-\zeta}{1+r_1}$ , which results in

$$\zeta \geq \frac{r_1\xi + 1 - \xi}{2r_1\xi + 1}.$$

The latter condition is equivalent to  $1 - 2\zeta - \frac{1-\zeta}{r_1+1} \leq 0$ , which is

$$\zeta \geq \frac{r_1}{2r_1 + 1}.$$

It is not difficult to see

$$\frac{r_1}{2r_1 + 1} > \frac{r_1\xi + 1 - \xi}{2r_1\xi + 1}$$

for  $\xi > 1$ . As a result, the condition on  $\zeta$  is

$$\frac{r_1}{2r_1 + 1} \leq \zeta < 1. \quad (26)$$

If  $\eta_1 = T_1^{-\zeta}$  is taken to satisfy this condition, the optimal rate of  $\lambda_1$  is given by Eq. (24). For instance, if  $\zeta \in (1/3, 1)$ , this is always satisfied, since  $r_1 \in [1/2, 1]$ . The resulting generalization bound is given by

$$E\|g_{\Theta^{(T_1)}} - \varphi\|_{L^2(\rho_X)}^2 \leq \varepsilon + cT_1^{-\frac{2r_1(1-\zeta)}{r_1+1}} R_0^{\frac{r_1}{r_1+1}}. \quad (27)$$

**(I-B)  $r_1 > r_0$ :** In this case, (a0) is larger than (a1). By equating (a0) and (e), we have

$$\lambda_1 = T_1^{-\frac{1-\zeta}{r_0+1}} R_0^{\frac{1}{2r_0+2}}. \quad (28)$$

By a similar argument to the case (I-A), the condition on  $\zeta$  is

$$\max\left\{\frac{r_0}{2r_0 + 1}, \frac{(2r_1 - r_0)\xi + 1 - \xi}{2r_1\xi + 1}\right\} \leq \zeta < 1. \quad (29)$$

The generalization bound is given by

$$E\|g_{\Theta^{(T_1)}} - \varphi\|_{L^2(\rho_X)}^2 \leq \varepsilon + cT_1^{-\frac{2r_0(1-\zeta)}{r_0+1}} R_0^{\frac{r_0}{r_0+1}}. \quad (30)$$

**(Case II)  $T_1\lambda_1\eta_1^2 \gg 1$ : large learning rate.** Next, we consider the case where the regularization coefficient  $\eta_1$  is large so that  $T_1\lambda_1\eta_1^2 \gg 1$ , which includes the constant  $\eta_1$ . In this case, (b) is larger than (e).

**(II-A)  $r_0 \geq r_1$ .** In this case, (a1) is larger than (a0). By equating (a1) and (b), we have

$$\lambda_1 = T_1^{-\frac{1}{2r_1+1}} R_0^{\frac{1}{2r_1+1}}. \quad (31)$$

The conditions are  $\lambda_1 \gg T_1^{-\frac{\xi}{2r_1\xi+1}}$  and  $T_1\lambda_1\eta_1^2 \gg 1$ . The former condition always holds for  $\xi > 1$ , and the latter is equivalent to  $\zeta \leq \frac{r_1}{2r_1+1}$ . As a result, under the condition

$$\zeta \leq \frac{r_1}{2r_1 + 1}, \quad (32)$$

the generalization bound is given by

$$E\|g_{\Theta^{(T_1)}} - \varphi_0\|_{L^2(\rho_X)}^2 \leq \varepsilon + cT_1^{-\frac{2r_1}{2r_1+1}} R_0^{\frac{2r_1}{2r_1+1}}. \quad (33)$$

**(II-B)  $r_1 > r_0$ :** In this case, (a0) is larger than (a1). By equating (a0) and (b), we have

$$\lambda_1 = T_1^{-\frac{1}{2r_0+1}} R_0^{\frac{1}{2r_0+1}}. \quad (34)$$

The conditions  $\lambda_1 \gg T_1^{-\frac{\xi}{2r_1\xi+1}}$  and  $T_1\lambda_1\eta_1^2 \gg 1$  are respectively  $r_1 \leq r_0 + \frac{\xi-1}{2\xi}$  and  $\zeta \leq \frac{r_0}{2r_0+1}$ . Thus, under the conditions

$$\zeta \leq \frac{r_0}{2r_0 + 1}, \quad r_0 < r_1 \leq r_0 + \frac{\xi-1}{2\xi}, \quad (35)$$

the generalization bound is

$$E\|g_{\Theta^{(T_1)}} - \varphi_0\|_{L^2(\rho_X)}^2 \leq \varepsilon + cT_1^{-\frac{2r_0}{2r_0+1}} R_0^{\frac{2r_0}{2r_0+1}}. \quad (36)$$

In summary, the generalization bounds in various conditions are summarized in Table 1.

$r_0, r_1$	$\eta_1 = T^{-\zeta}$	Bound
$r_0 \geq r_1$	$\frac{r_1}{2r_1+1} \leq \zeta < 1$	$\varepsilon + c' \left( c + T_0^{-\frac{2r_0\xi}{2r_0\xi+1} \cdot \frac{r_1}{r_1+1}} \right) T_1^{-\frac{2r_1(1-\zeta)}{r_1+1}}$
$r_0 < r_1$	$\max \left\{ \frac{r_0}{2r_0+1}, \frac{(2r_1-r_0)\xi+1-\xi}{2r_1\xi+1} \right\} \leq \zeta < 1$	$\varepsilon + c' \left( c + T_0^{-\frac{2r_0\xi}{2r_0\xi+1} \cdot \frac{r_0}{r_0+1}} \right) T_1^{-\frac{2r_0(1-\zeta)}{r_0+1}}$
$r_0 \geq r_1$	$\zeta \leq \frac{r_1}{2r_1+1}$	$\varepsilon + c' \left( c + T_0^{-\frac{2r_0\xi}{2r_0\xi+1} \cdot \frac{2r_1}{2r_1+1}} \right) T_1^{-\frac{2r_1}{2r_1+1}}$
$r_0 < r_1 \leq r_0 + \frac{\xi-1}{2\xi}$	$\zeta \leq \frac{r_0}{2r_0+1}$	$\varepsilon + c' \left( c + T_0^{-\frac{2r_0\xi}{2r_0\xi+1} \cdot \frac{2r_0}{2r_0+1}} \right) T_1^{-\frac{2r_0}{2r_0+1}}$

Table 1: Generalization bounds in various conditions.

## E.6 Proof of Theorem 2

The proof of Theorem 2 is based on the application of the theory in [45] to the fine-tuning phase, adapting the initialization given by the result of pre-training  $\hat{\varphi}_0$ .

In the sequel, we focus on the fine-tune with  $T_1$  samples with  $y_t = \varphi(x_t)$ . Recall that

$$\varphi(x) = \varphi_0(x) + \varphi_1(x).$$

### E.6.1 Reference ASGD on RKHS

We use a surrogate sequence of functions in an RKHS for the proof. Let  $k_M$  be the random feature approximation of the TNK  $k_\infty$ , i.e.,

$$k_M(x, x') = \frac{1}{M} \sum_{r=1}^M \sigma(b_r^T x) \sigma(b_r^T x') + \frac{x^T x'}{M} \sum_{r=1}^M \sigma'(b_r^T x) \sigma'(b_r^T x'), \quad (37)$$

where  $(b_r)_{r=1}^M$  is i.i.d. random sample from the uniform distribution on the unit sphere  $\mathbb{S}^{d-1}$ . The associated RKHS is denoted by  $\mathcal{H}_M$ .

A reference ASGD is defined by the following update rule of functions in the RKHS  $\mathcal{H}_M$ :

$$g^{(t+1)} = (1 - \eta\lambda)g^{(t)} - \eta(g^{(t)}(x_t) - y_t)k_M(\cdot, x_t), \quad (t = 0, \dots, T-1) \quad (38)$$

with the initialization given by  $g^{(0)} := \hat{\varphi}_0$ . The average is taken at the final step:

$$\bar{g}^{(T_1)} := \frac{1}{T_1 + 1} \sum_{t=0}^{T_1} \alpha_t g^{(t)}. \quad (39)$$

By considering continual learning of pre-train and fine-tune, we have the following proposition [45, Proposition A].

**Proposition 3.** *Assume (A1) and (A2). Suppose that  $\eta_1 \lambda_1 < 1$ . Then for any  $T_1 \in \mathbb{N}$  and  $\varepsilon > 0$ , there is  $M_* = M_*(T_1, \varepsilon) \in \mathbb{N}$  such that during the fine-tune learning*

$$\|g^{(t)} - g_{\Theta^{(t)}}\|_{L^\infty(\rho_X)} \leq \varepsilon, \quad (40)$$

holds for any  $M \geq M_*$  and  $0 \leq t \leq T_1$ .

This proposition shows that, if we use a very wide network, the learning of ASGD in the parameter space can be approximated by the reference ASGD on the RKHS with negligible error.

The generalization bound will be given by the following decomposition:

$$\|g_{\Theta^{(T_1)}} - \varphi\|_{L^2(\rho_X)}^2 \leq 2\|g_{\Theta^{(T_1)}} - \bar{g}^{(T_1)}\|_{L^2(\rho_X)}^2 + 2\|\bar{g}^{(T_1)} - \varphi\|_{L^2(\rho_X)}^2, \quad (41)$$

in which the first term of the right hand side is bounded by Proposition 3 with an arbitrary small value  $\varepsilon$  for large  $M$ . The second term will be discussed in the next subsection.

### E.6.2 Convergence rates of reference ASGD

The covariance operators for  $\mathcal{H}_\infty$  and  $\mathcal{H}_M$  are denoted by  $\Sigma_\infty$  and  $\Sigma_M$ , respectively;

$$\begin{aligned}\Sigma_\infty &:= E_{\rho_X}[k_\infty(\cdot, X) \otimes k_\infty(\cdot, X)^*], \\ \Sigma_M &:= E_{\rho_X}[k_M(\cdot, X) \otimes k_M(\cdot, X)^*],\end{aligned}\tag{42}$$

or equivalently,

$$\Sigma_\infty f = \int k_\infty(\cdot, x) f(x) d\rho_X(x), \quad \Sigma_M h = \int k_M(\cdot, x) h(x) d\rho_X(x),$$

for  $f \in \mathcal{H}_\infty, h \in \mathcal{H}_M$ . The regularized target functions  $\varphi_{M,\lambda}^{(i)}$  ( $i = 0, 1$ ) are defined by

$$\varphi_{M,\lambda}^{(i)} := (\Sigma_M + \lambda I)^{-1} \Sigma_M \varphi_i \quad (i = 0, 1).\tag{43}$$

$\varphi_{\infty,\lambda}^{(i)}$  is defined similarly with  $\Sigma_\infty$ . Note that  $\varphi_{M,\lambda} := (\Sigma_M + \lambda I)^{-1} \Sigma_M \varphi = \varphi_{M,\lambda}^{(0)} + \varphi_{M,\lambda}^{(1)}$ .

First, we decompose  $\|\bar{g}^{(T_1)} - \varphi\|_{L^2(\rho_X)}^2$  by

$$\begin{aligned}\|\bar{g}^{(T_1)} - \varphi\|_{L^2(\rho_X)}^2 &= \|\bar{g}^{(T_1)} - \varphi_{M,\lambda} + \varphi_{M,\lambda}^{(0)} + \varphi_{M,\lambda}^{(1)} - \varphi_0 - \varphi_1\|_{L^2(\rho_X)}^2 \\ &\leq 3\|\bar{g}^{(T_1)} - \varphi_{M,\lambda}\|_{L^2(\rho_X)}^2 + 3\|\varphi_{M,\lambda}^{(0)} - \varphi_0\|_{L^2(\rho_X)}^2 + 3\|\varphi_{M,\lambda}^{(1)} - \varphi_1\|_{L^2(\rho_X)}^2.\end{aligned}$$

The second and third terms are known to have a bound [45, Propositions C and D]

$$\|\varphi_{\infty,\lambda}^{(i)} - \varphi_i\|_{L^2(\rho_X)}^2 \leq \varepsilon + \lambda^{2r_i} \|\Sigma_\infty^{-r_i} \varphi_i\|_{L^2(\rho_X)}^2, \quad (i = 0, 1),\tag{44}$$

where  $\varepsilon$  is arbitrarily small for large  $M$ . We have thus

$$\|\bar{g}^{(T_1)} - \varphi\|_{L^2(\rho_X)}^2 \leq \varepsilon + 3\|\bar{g}^{(T_1)} - \varphi_{M,\lambda}\|_{L^2(\rho_X)}^2 + 3\lambda^{2r_0} \|\Sigma_\infty^{-r_0} \varphi_0\|_{L^2(\rho_X)}^2 + 3\lambda^{2r_1} \|\Sigma_\infty^{-r_1} \varphi_1\|_{L^2(\rho_X)}^2.\tag{45}$$

As shown in [45], the term  $\|\bar{g}^{(T_1)} - \varphi_{M,\lambda}\|_{L^2(\rho_X)}^2$  can be analyzed by the bias and noise terms of the stochastic recursion on RKHS Eq. (38), which is rewritten as

$$g^{(t+1)} = (I - \eta H_t - \eta \lambda I) g^{(t)} + \eta y_t k_M(\cdot, x_t),\tag{46}$$

where

$$H_t := k_M(\cdot, x_t) \otimes k_M(\cdot, x_t)^*,$$

is a one-sample estimate of  $\Sigma_M$ . By subtracting  $\varphi_{M,\lambda}$  from both hand sides, we have

$$g^{(t+1)} - \varphi_{M,\lambda} = (I - \eta H_t - \eta \lambda I)(g^{(t)} - \varphi_{M,\lambda}) + \beta_t,\tag{47}$$

where

$$\beta_t = \eta y_t k_M(\cdot, x_t) - \eta(H_t + \lambda I)(\Sigma_M + \lambda I)^{-1} \Sigma_M \varphi_{M,\lambda}$$

is the zero mean noise term. Using this recursive formula, Nitanda and Suzuki [45] derives a bound:

$$\begin{aligned}\|\bar{g}^{(T)} - \varphi_{M,\lambda}\|_{L^2(\rho_X)}^2 &\leq \frac{c_1}{T_1 + 1} \|(\Sigma_M + \lambda I)^{-1/2} (g^{(0)} - \varphi_{M,\lambda})\|_{L^2(\rho_X)}^2 \\ &\quad + \frac{c_2}{(T_1 + 1)^2 \eta^2} \|(\Sigma_M + \lambda I)^{-1} (g^{(0)} - \varphi_{M,\lambda})\|_{L^2(\rho_X)}^2 \\ &\quad + \frac{c_3}{T_1 + 1} (1 + \|\varphi\|_{L^2(\rho_X)}^2 + 24\|\Sigma_\infty^{-r_1} \varphi\|_{L^2(\rho_X)}^2) \text{Tr}[\Sigma_M (\Sigma_M + \lambda I)^{-1}].\end{aligned}\tag{48}$$

To bound this expression further, we use Proposition B in [45]

$$\|(\Sigma_M + \lambda I)^{-1/2} \varphi_{M,\lambda}^{(i)}\|_{L^2(\rho_X)}^2 \leq 2\|\varphi_i\|_{\mathcal{H}_\infty}^2,$$

as well as Proposition C in [45], which states that under the assumptions (A1)-(A3) for any  $\varepsilon, \lambda$  and  $0 < \delta \leq 1$ , there is  $M_0 = M_0(\varepsilon, \delta, \lambda)$  such that for any  $M \geq M_0$

$$\|\varphi_{M,\lambda}^{(i)} - \varphi_{\infty,\lambda}^{(i)}\|_{L^2(\rho_X)}^2 \leq \varepsilon,$$

with probability larger than  $1 - \delta$ . Then, we obtain, with high probability, that

$$\begin{aligned}
& \|(\Sigma_M + \lambda I)^{-1/2}(g^{(0)} - \varphi_{M,\lambda})\|_{L^2(\rho_X)}^2 \\
& \leq 4\|(\Sigma_M + \lambda I)^{-1/2}(\hat{\varphi}_0 - \varphi_0)\|_{L^2(\rho_X)}^2 + 4\|(\Sigma_M + \lambda I)^{-1/2}(\varphi_0 - \varphi_{\infty,\lambda}^{(0)})\|_{L^2(\rho_X)}^2 \\
& \quad + 4\|(\Sigma_M + \lambda I)^{-1/2}(\varphi_{\infty,\lambda}^{(0)} - \varphi_{M,\lambda}^{(0)})\|_{L^2(\rho_X)}^2 + 4\|(\Sigma_M + \lambda I)^{-1/2}\varphi_{M,\lambda}^{(1)}\|_{L^2(\rho_X)}^2 \\
& \leq \frac{4}{\lambda}\|\hat{\varphi}_0 - \varphi_0\|_{L^2(\rho_X)}^2 + \frac{4}{\lambda}\lambda^{2r_0}\|\varphi_0\|_{L^2(\rho_X)}^2 + \varepsilon_M + 8\|\varphi_1\|_{\mathcal{H}_\infty}^2,
\end{aligned} \tag{49}$$

where we use Eq. (44) in the second term in the last inequality. Similarly, with high probability, we have

$$\begin{aligned}
& \|(\Sigma_M + \lambda I)^{-1}(g^{(0)} - \varphi_{M,\lambda})\|_{L^2(\rho_X)}^2 \\
& \leq 4\|(\Sigma_M + \lambda I)^{-1}(\hat{\varphi}_0 - \varphi_0)\|_{L^2(\rho_X)}^2 + 4\|(\Sigma_M + \lambda I)^{-1}(\varphi_0 - \varphi_{\infty,\lambda}^{(0)})\|_{L^2(\rho_X)}^2 \\
& \quad + 4\|(\Sigma_M + \lambda I)^{-1}(\varphi_{\infty,\lambda}^{(0)} - \varphi_{M,\lambda}^{(0)})\|_{L^2(\rho_X)}^2 + 4\|(\Sigma_M + \lambda I)^{-1}\varphi_{M,\lambda}^{(1)}\|_{L^2(\rho_X)}^2 \\
& \leq \frac{4}{\lambda^2}\|\hat{\varphi}_0 - \varphi_0\|_{L^2(\rho_X)}^2 + \frac{4}{\lambda^2}\lambda^{2r_0}\|\varphi_0\|_{L^2(\rho_X)}^2 + \varepsilon_M + \frac{8}{\lambda}\|\varphi_1\|_{\mathcal{H}_\infty}^2
\end{aligned} \tag{50}$$

It is also known [45, Proposition B] that, for  $\lambda \leq \|\Sigma_\infty\|$ ,

$$\text{Tr}[\Sigma_M(\Sigma_M + \lambda I)^{-1}] \leq 3\text{Tr}[\Sigma_\infty(\Sigma_\infty + \lambda I)^{-1}]. \tag{51}$$

Combining Eqs.(45), (48), (49), (50), and (51), we obtain the result.